IJMMM International Journal of Minerals, Metallurgy and Materials 矿物冶金与材料学报（英文版）

A review on the multi-scaled structures and mechanical/thermal properties of tool steels fabricated by laser powder bed fusion additive manufacturing

Huajing Zong, Nan Kang, Zehao Qin, and Mohamed El Mansori

Cite this article as:
Huajing Zong, Nan Kang, Zehao Qin, and Mohamed El Mansori, A review on the multi-scaled structures and mechanical/thermal properties of tool steels fabricated by laser powder bed fusion additive manufacturing, *Int. J. Miner. Metall. Mater.*, 31(2024), No. 5, pp. 1048-1071. https://doi.org/10.1007/s12613-023-2731-5

View the article online at SpringerLink or IJMMM Webpage.

Articles you may be interested in

De-cheng Kong, Chao-fang Dong, Xiao-qing Ni, Liang Zhang, Rui-xue Li, Xing He, Cheng Man, and Xiao-gang Li, Microstructure and mechanical properties of nickel-based superalloy fabricated by laser powder-bed fusion using recycled powders, *Int. J. Miner. Metall. Mater.*, 28(2021), No. 2, pp. 266-278. https://doi.org/10.1007/s12613-020-2147-4

Yi-li Dai, Sheng-fu Yu, An-guo Huang, and Yu-sheng Shi, Microstructure and mechanical properties of high-strength low alloy steel by wire and arc additive manufacturing, *Int. J. Miner. Metall. Mater.*, 27(2020), No. 7, pp. 933-942. https://doi.org/10.1007/s12613-019-1919-1

Yi-wa Luo, Ming-yong Wang, Ji-guo Tu, Yu Jiang, and Shu-qiang Jiao, Reduction of residual stress in porous Ti6Al4V by *in situ* double scanning during laser additive manufacturing, *Int. J. Miner. Metall. Mater.*, 28(2021), No. 11, pp. 1844-1853. https://doi.org/10.1007/s12613-020-2212-z

Hong-yu Chen, Dong-dong Gu, Qing Ge, Xin-yu Shi, Hong-mei Zhang, Rui Wang, Han Zhang, and Konrad Kosiba, Role of laser scan strategies in defect control, microstructural evolution and mechanical properties of steel matrix composites prepared by laser additive manufacturing, *Int. J. Miner. Metall. Mater.*, 28(2021), No. 3, pp. 462-474. https://doi.org/10.1007/s12613-020-2133-x

Mehmet Akif Erden and Fatih Aydın, Wear and mechanical properties of carburized AISI 8620 steel produced by powder metallurgy, *Int. J. Miner. Metall. Mater.*, 28(2021), No. 3, pp. 430-439. https://doi.org/10.1007/s12613-020-2046-8

Dong Wu, Wen-ya Li, Yan-jun Gao, Jun Yang, Quan Wen, Nektarios Vidakis, and Achillefs Vairis, Impact of travel speed on the microstructure and mechanical properties of adjustable-gap bobbin-tool friction stir welded Al–Mg joints, *Int. J. Miner. Metall. Mater.*, 28(2021), No. 4, pp. 710-717. https://doi.org/10.1007/s12613-020-2134-9

IJMMM WeChat

QQ author group

INTERNATIONAL JOURNAL OF
Minerals, Metallurgy and Materials

Volume 31, Number 5, May 2024
Page 1048

Invited Review https://doi.org/10.1007/s12613-023-2731-5

A review on the multi-scaled structures and mechanical/thermal properties of tool steels fabricated by laser powder bed fusion additive manufacturing

Huajing Zong[1)], *Nan Kang*[1),✉], *Zehao Qin*[1)], *and Mohamed El Mansori*[1,2)]

1) Arts et Metiers Institute of Technology, MSMP, HESAM Université, Châlons-en-Champagne F-51006, France
2) Texas A & M Engineering Experiment Station, Institute for Manufacturing Systems, College Station TX77843, USA
(Received: 29 April 2023; revised: 18 July 2023; accepted: 22 August 2023)

Abstract: The laser powder bed fusion (LPBF) process can integrally form geometrically complex and high-performance metallic parts that have attracted much interest, especially in the molds industry. The appearance of the LPBF makes it possible to design and produce complex conformal cooling channel systems in molds. Thus, LPBF-processed tool steels have attracted more and more attention. The complex thermal history in the LPBF process makes the microstructural characteristics and properties different from those of conventional manufactured tool steels. This paper provides an overview of LPBF-processed tool steels by describing the physical phenomena, the microstructural characteristics, and the mechanical/thermal properties, including tensile properties, wear resistance, and thermal properties. The microstructural characteristics are presented through a multiscale perspective, ranging from densification, meso-structure, microstructure, substructure in grains, to nanoprecipitates. Finally, a summary of tool steels and their challenges and outlooks are introduced.

Keywords: additive manufacturing; laser powder bed fusion; tool steel; multi-scaled structure; mechanical properties; thermal properties

1. Introduction

Tool steels are a type of material developed for manufacturing tools, dies and molds, which are required to have good high-temperature strength, hardness, and friction resistance. Currently, most tool steels are produced by conventional manufacturing technologies such as casting and welding and powder metallurgy in the tool- and die-making industries [1]. After long-term research and exploration, traditional methods employed in the preparation of tool steels are well established. By precisely controlling the process parameters and post-treatment procedures, it is possible to effectively control the microstructure of tool steels and achieve the desired properties. Furthermore, traditional manufacturing techniques are suitable for high-volume production of components with simple structures [2–3]. Nevertheless, these conventional methods face limitations in fabricating intricate structures. The fabrication of complex components using traditional methods requires the separate processing and assembly of various parts, inevitably resulting in increased material costs and time consumption [1]. As the complexity and requirements for quality and efficiency in preparing workpieces increase, conventional manufacturing methods gradually fail to meet the requirements.

Recently, laser powder bed fusion (LPBF) has shown great potential in making complex components. In the LPBF process, a layer of powder with a predetermined thickness is evenly spread onto the build plate. According to the digital model, the laser beam selectively melts the powder particles layer by layer [4]. The LPBF process offers high design freedom, enabling the production of complex components that are unattainable using conventional manufacturing methods. Additionally, the near-net-shape forming characteristic of the LPBF process enhances the efficiency and cost-effectiveness in manufacturing complex structural components [5]. For example, the cooling channel in traditional molds typically follows a straight path with a circular cross-section, leading to uneven cooling rates and resulting in warping and deformation. The introduction of LPBF enables the production of conformal cooling channels within the molds [6]. However, LPBF is a multi-physical process that exhibits different time-temperature profiles compared to conventional manufacturing techniques, resulting in diverse microstructures, defects, and mechanical properties [7]. This also means that achieving consistent and high-quality components in LPBF is complex and requires precise process control. In addition, due to the relatively short development time of the LPBF process, the range of materials suitable for these processes is still somewhat limited. Although there are many types of tool steels available for conventional methods, the current research and application in LPBF technology are primarily focused on carbon-bearing steels and maraging steels [8]. The high cooling rates in the LPBF process result in fine microstructures, cellular substructures, and high dislocation density, contributing to a slightly higher tensile strength in LPBF-processed tool steels compared to conventional tool steels.

✉ Corresponding author: Nan Kang E-mail: nan.kang@ensam.eu
© University of Science and Technology Beijing 2024

The layer-by-layer deposition technique in LPBF generates repeated thermal cycles, which induce both phase transitions and precipitation behavior [9–13]. The formation of retained austenite and precipitates in LPBF-processed carbon-bearing tool steels could improve the mechanical properties. Simultaneously, the rapid cooling rate and the martensite transformation during the cooling process tend to increase the residual stress. In the case of carbon-bearing tool steels, high residual stress leads to brittle fracture of the martensite matrix. While the LPBF process facilitates the production of maraging steels with ductile martensite compared to carbon-bearing tool steel, the presence of residual stress also affects the properties [12]. Moreover, LPBF is a highly complex process involving multiple physical phenomena at different scales. This poses challenges in controlling the quality of the formed components [14]. There are significant variations in the microstructure and properties among LPBF-processed tool steels [8]. The retained austenite in carbon-bearing tool steel with different volume fractions, compositions, morphologies, and sizes exhibits varying effects on the deformation mechanism [11,15]. For instance, retained austenite characterized by high carbon content and a long film-like morphology promotes the initiation and propagation of cracks [11]. In the case of maraging tool steels, it is uncertain whether intrinsic heat treatment (Intrinsic-HT) can induce precipitation [3,13]. Achieving high-quality tool steels through the LPBF process requires a comprehensive understanding of the underlying physical phenomena, microstructural evolution, and influence of microstructures on properties. Moreover, the wear behavior and thermal properties of tool steels play a critical role in determining the service life, production efficiency, and mold quality. However, there is currently a lack of comprehensive summaries regarding these aspects. Therefore, this reviewed paper first introduces the physical phenomenon in the LPBF process. Then, a systematic and comprehensive review of the microstructural characteristics of tool steels (including maraging tool steels and carbon-bearing tool steels) is conducted from a multiscale perspective. This encompasses densification, meso-structure, microstructure, and substructure in grains and nanostructures. Subsequently, the review delves into the tensile property, wear behavior, and thermal property. Finally, the review concludes with a summary and outlook on tool steels fabricated by the LPBF process.

2. Featured physical phenomenon in the LPBF process

The LPBF process involves several key steps. First, powder particles are evenly spread onto the powder bed. Then, the laser beam is directed onto the powder bed, melting the powder particles to form a molten pool. As the laser beam moves away, the temperature of the molten pool decreases, and the materials solidify. During subsequent passes of the laser beam, the solidified materials undergo repeated thermal cycles, which play a crucial role in adjusting the microstructures [16]. In the following section, we will elaborate on the physical phenomena associated with the laser-powder bed interaction, the behavior of the molten pool, and the solidification process, shedding light on the influence on the final microstructural characteristics of the fabricated components.

2.1. Physical phenomena in the laser-powder bed interaction

The efficient absorption of laser beams by powder depends on a combination of factors, including the heat source characteristics, the powder layer characteristics, and the laser-powder interaction. To describe the heat source characteristics, various heat source models have been proposed. It was found that the exponential decay equation method more accurately describes the actual heat source [17]. In the exponentially decaying equation method, the laser power density decays exponentially with distance from the laser spot center in the horizontal plane, and the laser power density still decays exponentially with increasing depth in the vertical plane [18–19]. The Gaussian distribution of laser intensity induces the formation of directional thermal flux and influences the microstructure of parts. In addition to the laser source characteristics, the powder layer characteristics, including the surface chemistry, flowability, packing density, and thermal properties such as absorptivity and conductivity, also influence the absorption rate of powder particles to the laser beam and the forming quality [5]. The different powder particle morphologies led to pores and higher porosity in parts. Powder particles with near-spherical shapes and a broader size distribution, containing a substantial amount of fine particles, tend to have large packing density and ensure part densification [20]. A high packing density contributes to an increase in the thermal absorptivity and thermal conductivity of the powder bed. The combination of high thermal absorptivity and thermal conductivity can enhance solidification rates and temperature gradients, leading to the formation of refined microstructures and improved mechanical properties. However, it is important to note that these factors may also result in the development of residual stresses. The high oxygen content not only degrades the flowability and packing density but also increases the likelihood of defects, including balling and surface roughness formation. The high oxygen content in molten metals promotes oxidation reactions, which can potentially lead to component oxidation and affect the mechanical properties [21]. The laser-powder interaction also impacts the melt pool. During the interaction between the laser and the powder, a laser beam with a specific energy distribution reaches the powder bed. A portion of the laser is absorbed by the powder particles, while the remaining portion is either reflected away from the powder bed or its intensity becomes negligible after multiple reflections. The laser not only melts the powder particles on the surface of the powder bed but also penetrates to a certain depth [4]. As the powder particles absorb the energy of the laser beam and gradually melt, heat dissipation occurs in different ways by thermal conduction, thermal convection, and thermal radiation [22]. When the molten pool temperature is higher than

the evaporation temperature of the material, the material evaporates and removes part of the heat [23]. With further consideration of the metal convection in the molten pool (which will be discussed later), the molten metal convection in the molten pool has an impact on heat dissipation [18].

2.2. Physical phenomenon in the molten pool

The shape of the molten pool and the flow of the molten metal are affected by the buoyancy force, gravity, surface tension (capillary force and Marangoni effect), and recoil pressure, as shown in Fig. 1 [19]. The capillary force is perpendicular to the liquid surface and increases as the temperature decreases, which is usually considered to be equivalent to the external pressure. The smaller the radius of curvature is, the greater the capillary force. The Marangoni force is parallel to the liquid surface and is the variation in surface tension with temperature. In other words, the Marangoni force promotes the liquid metal from areas with low surface tension to areas with high surface tension. In the case of materials containing few surface-active elements, the negative surface tension gradient promoted the flow of molten metal from the high-temperature area in the middle area to the edge of the molten pool, which induced the molten pool to become wide and shallow. The high content of surface-active content in materials, such as the high content of sulfur in SS316L, changed the surface tension gradient to positive. Consequently, the flow of molten metal shifted towards an inwards radial direction, leading to the formation of a deep and narrow molten pool [4,24]. Buoyancy arises from spatial variations in the density of liquid metal, primarily caused by temperature changes and, to a lesser extent, local composition variations. The higher temperature at the upper part of the molten pool results in an upwards movement of the low-density liquid metal. Simultaneously, gravity induces fluid flow in the opposite direction. The influence of buoyancy forces and gravity on heat transfer and fluid flow can be neglected compared to the Marangoni effect [25]. It can also be seen that buoyancy and gravity are not taken into account in the majority of studies on the simulation of molten pool behavior during the LPBF process. The evaporated material not only removes part of the heat but also generates greater recoil pressure on the molten pool. The recoil force acts perpendicular to the free surface of the molten pool and exerts a

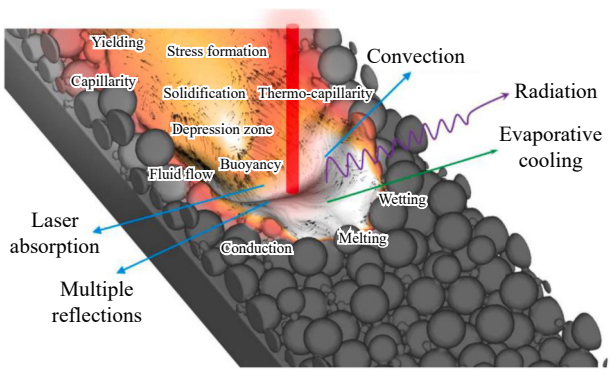

Fig. 1. Schematic illustration of the physical phenomenon in the molten pool during the LPBF process [19].

downwards pressure on the liquid, resulting in the formation of a narrow and deep molten pool with a lower surface temperature [26]. In simulating the molten pool behavior, neglecting the recoil pressure made the simulated depth of the molten pool less than the actual depth, especially in the high laser powder density condition [23].

2.3. Physical phenomenon in the solidified material

The evolution of the grain structure of solidified material, including grain size, morphology, and growth direction, determines the microstructural characteristics and mechanical performance of the parts [4]. In the LPBF process, nucleation mainly occurs at the molten pool boundaries through heterogeneous nucleation. The heterogeneous nucleation mechanism is favored due to the significantly lower energy barrier compared to homogeneous nucleation [27]. Following heterogeneous nucleation at the molten pool boundaries, grains with random orientations grow at a specific rate through epitaxial growth. The direction of grain growth is typically perpendicular to the molten pool boundaries, aligning with the maximum heat dissipation flow [28]. The preferred crystallographic direction of the grains with the same orientation as or close to the maximum temperature gradient has the fastest growth rate, and the grains with other orientations gradually stop. This phenomenon is referred to as competitive growth, which leads to the formation of texture [27]. Grain size and morphology are influenced by the temperature gradient (G) and growth rate (R). The temperature field and gradient can be simulated using various models. With the increase in physical phenomena considered, the simulated temperature field is closer to the real temperature field. At the same time, the required calculation cost increases, and the calculation efficiency decreases. As shown in Fig. 2(a)–(b), the simulated molten pool in LPBF-processed H13 steel, using the heat flow model at the powder scale, closely matches the real experimental results [29]. For the growth rate, there are different grain growth models describing the relationship between the dendrite tip growth rate and undercooling. Among these models, the Kurz-Giovanola-Trivedi (KGT) model is widely employed by researchers, particularly for simulating the directional growth of dendrites in the LPBF process with high growth rates [30]. Alternatively, for the sake of simplicity, the relationship between total undercooling and dendrite tip growth rate can be approximated using a polynomial function based on experimental results [31]. By combining the temperature field and dendritic tip growth model, the simulated microstructure of 316L stainless steel in the LPBF process showed good correspondence with the experimental results, as depicted in Fig. 2(c)–(d) [32]. In addition, the calculated temperature gradient (G) and growth rate (R) could be used to design the microstructure. Fig. 2(e) illustrates the correlation between G, R, and the resulting microstructure. The product of $G \times R$ represents the cooling rate that controls the grain size. A finer grain structure could be obtained at high cooling rates. On the other hand, the ratio of G/R determines the grain morphology. As the G/R decreases, the grain morphology changes from a planar front to

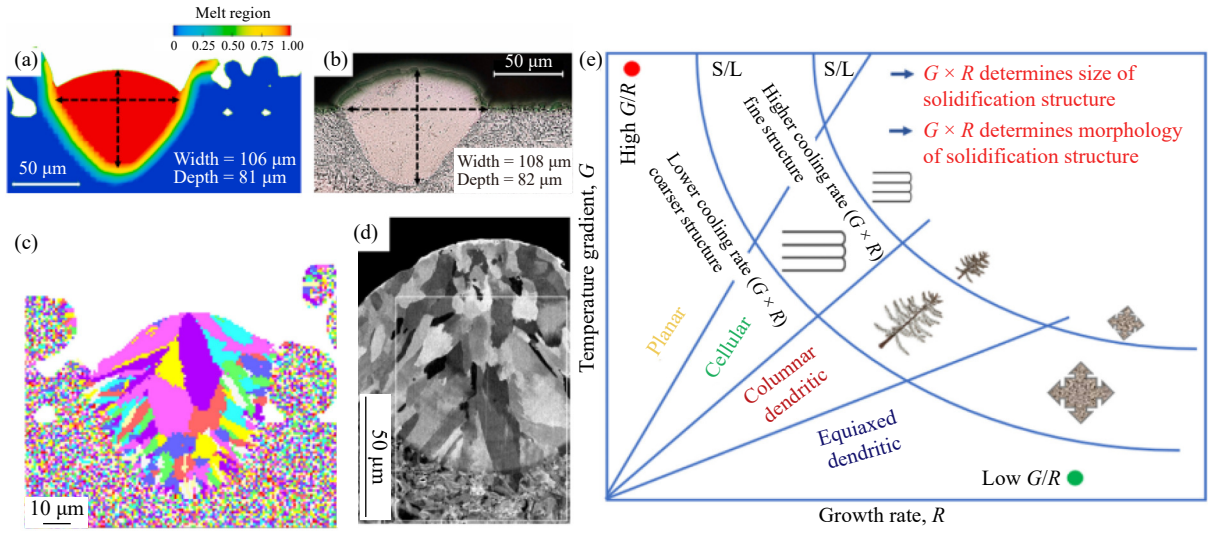

Fig. 2. (a) Simulated result and (b) experimental result of molten pool in LPBF-processed H13 steel [29]; (c) simulated result and (d) experimental result of the microstructure in the LPBF-processed 316L stainless steel. Reprinted from *Addit. Manuf.*, 28, Y. Zhang and J. Zhang, Modeling of solidification microstructure evolution in laser powder bed fusion fabricated 316L stainless steel using combined computational fluid dynamics and cellular automata, 750, Copyright 2019, with permission from Elsevier; (e) effect of the temperature gradient *G* and growth rate *R* on the morphology and size of the solidification microstructure [1].

equiaxed dendrites [1]. During laser melting of neighboring tracks and layers, the solidified materials undergo repeated thermal cycles. Repeated thermal cycles can induce solid-state transformations and the formation of residual tensile stress, influencing the microstructural characteristics and mechanical properties.

3. Microstructure characteristics of LPBF-processed tool steels

Two types of tool steels are widely used in the LPBF process: carbon-free maraging steels and carbon-bearing tool steels. Among maraging steels, 18Ni300 steel has been the subject of extensive research. However, other types of maraging steels, including 18Ni-250 [33], 14Ni-200 [34], and Fe–19Ni–*x*Al [35], have received less attention. For carbon-bearing tool steels, research has been conducted on M2 and HS 6-5-3-8 high-speed steels [36–37], as well as H11 and H13 hot work tool steels [38]. The majority of articles predominantly focus on H13 tool steel, and the observed phenomena are representative of the entire category of carbon-bearing tool steels. Due to the limitations in the length of the article, our paper will primarily concentrate on 18Ni300 as a representative maraging steel and H13 as a representative carbon-bearing steel. This chapter mainly introduces the microstructural characteristics of tool steel prepared by the LPBF process from different scales.

3.1. Carbon tool steels (H13 tool steel)

3.1.1. Densification and meso-structure

H13 steel is a typical hot working tool steel. The good high-temperature mechanical properties and low cost make it widely used in injection molds, shot extrusion, forging, and die casting. However, producing H13 steel using the LPBF process is somewhat challenging. The high thermal gradients and solid-state martensite transformations lead to the generation of high residual stress and cracking [39–41]. Savrai *et al.* [42] only adjusted the scan speed, and laser power cannot prevent crack formation. Many researchers preheated the baseplate to reduce the thermal gradient and prohibited crack formation [43–44]. Fig. 3(a)–(b) shows that changing the exposure time alone cannot obtain H13 steel with full density and crack-free structure. However, preheating the base plate increases the relative densities to above 99.5% and reduces the crack density from 10 m/m^2 to zero as the preheating temperature increases from no preheating to 300°C [43]. There is an obvious *in-situ* tempering phenomenon in the LPBF-processed H13 steel, as shown in Fig. 3(c). The molten pool morphology of H13 steel in the vertical plane exhibits a characteristic fish-scale pattern with alternating dark and bright layers [9,45]. The darker areas corresponded to the heat-affected zones consisting of tempered martensite and more precipitates, and the brighter regions corresponded to the bottom of fusion zones with less extensive tempering [9]. The morphology of laser tracks on the horizontal surface in Fig. 3(d) can reflect the rationality of hatch spacing and scanning strategy.

3.1.2. Microstructure

In the microstructure section, we mainly introduce the phase constitutions and grain morphology of tool steels. The phase constitution in conventional manufacturing H13 steel is fine carbides distributed evenly in the martensite matrix [9]. The LPBF-processed H13 steel consisted of martensite and retained austenite. The retained austenite corresponded to white regions of Fig. 4(a)–(b), which are interdendritic (intercellular) and enriched with C, Cr, Mo, V, and Si elements. The different formation mechanisms of the residual austenite in LPBF-processed H13 steel were proposed. One perspective suggests that the formation of retained austenite is attributed to elemental segregation during the solidification pro-

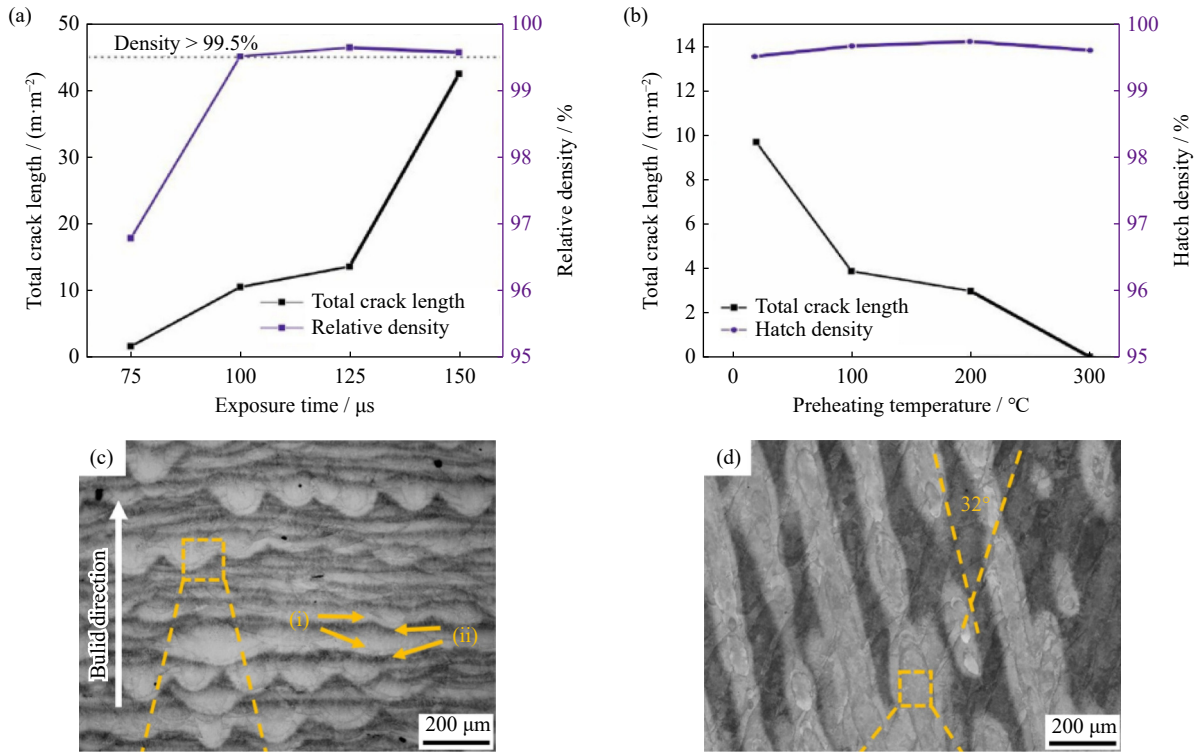

Fig. 3. Total crack length and relative density of LPBF-processed H13 steel at different (a) exposure times and (b) preheating temperatures. Reprinted from *J. Mater. Process. Technol.*, 255, J. Krell, A. Röttger, K. Geenen, and W. Theisen, General investigations on processing tool steel X40CrMoV5-1 with selective laser melting, 679, Copyright 2018, with permission from Elsevier; Meso-structure of the LPBF-processed H13 steel in the (c) build direction and (d) scanning direction. Reprinted from *Addit. Manuf.*, 34, E.B. Fonseca, A.H.G. Gabriel, L.C. Araújo, P.L.L. Santos, K.N. Campo, and E.S.N. Lopes, Assessment of laser power and scan speed influence on microstructural features and consolidation of AISI H13 tool steel processed by additive manufacturing, 101250, Copyright 2020, with permission from Elsevier.

cess [9–10,43,46–47]. It is a fact that the high cooling rate suppresses elemental diffusion and makes more carbon and alloying elements stay in the austenite matrix. The high content of carbon could effectively reduce the martensite transformation temperature [48]. The residual austenite contents in the building direction and horizontal direction were 8.7% and 6%, respectively, as depicted in Fig. 4(e)–(f). Li *et al.* [46] attributed the higher volume fraction of retained austenite in the build direction to the higher cooling rate in that direction compared to the horizontal direction. Another view about the formation mechanism of the retained austenite is the quenching and tempering process of the LPBF process. In the LPBF process, the molten pool initially solidifies into austenite. Due to the high cooling rate, when the temperature reaches the martensite transformation temperature, the austenite undergoes a martensitic transformation. During the melting of the overlying powder layer, the heat flow diffused to the deposited layers, leading to the retransformation of martensite into austenite. During the subsequent cooling process, the temperature cannot decrease to the martensitic finish temperature due to the continuous heat flow diffusing to the baseplate. Consequently, retained austenite is present in the LPBF-processed H13 steel [41,49]. Holzweissig *et al.* [49] believed that the higher content of retained austenite in the building direction was attributed to a longer building duration compared to the horizontal direction. Consequently, more carbon diffused from the carbon-supersaturated martensite into the untransformed austenite and stabilized larger fractions of austenite. Preheating the substrate increased the volume fraction of retained austenite in H13 steel [1,41,48,50]. At a preheating temperature of 200°C, the volume fraction of retained austenite was higher than that of the samples without preheating [44]. Mertens *et al.* [44] also found that when the preheating temperature increased to 400°C, the microstructure was bainite instead of martensite and austenite. The formation mechanism of retained austenite and how to control the volume fraction, morphology, and size remain uncertain. These features have a significant impact on the properties of H13 steel, and therefore, further investigation is needed.

The LPBF-processed H13 steel exhibits fine grains with a random distribution orientation, as depicted in Fig. 5(a)–(b). The weakening texture can be attributed to two main factors. One reason is that the martensite transformation destroyed the texture of columnar grains [11,51–52]. Fig. 5(c)–(d) illustrates that prior to the martensite transformation, the LPBF-processed H13 steel showed epitaxial growth of austenite grains along the building direction. However, during martensite transformation, the prior austenite transformed into several lath martensitic grains with varying habit planes [53]. Fig. 5(e) shows the microscopic structure of lath martensite composed of laths, blocks, and packets of a three-layer heterogeneous structure in morphology. A group of martensite laths with almost the same orientation forms a

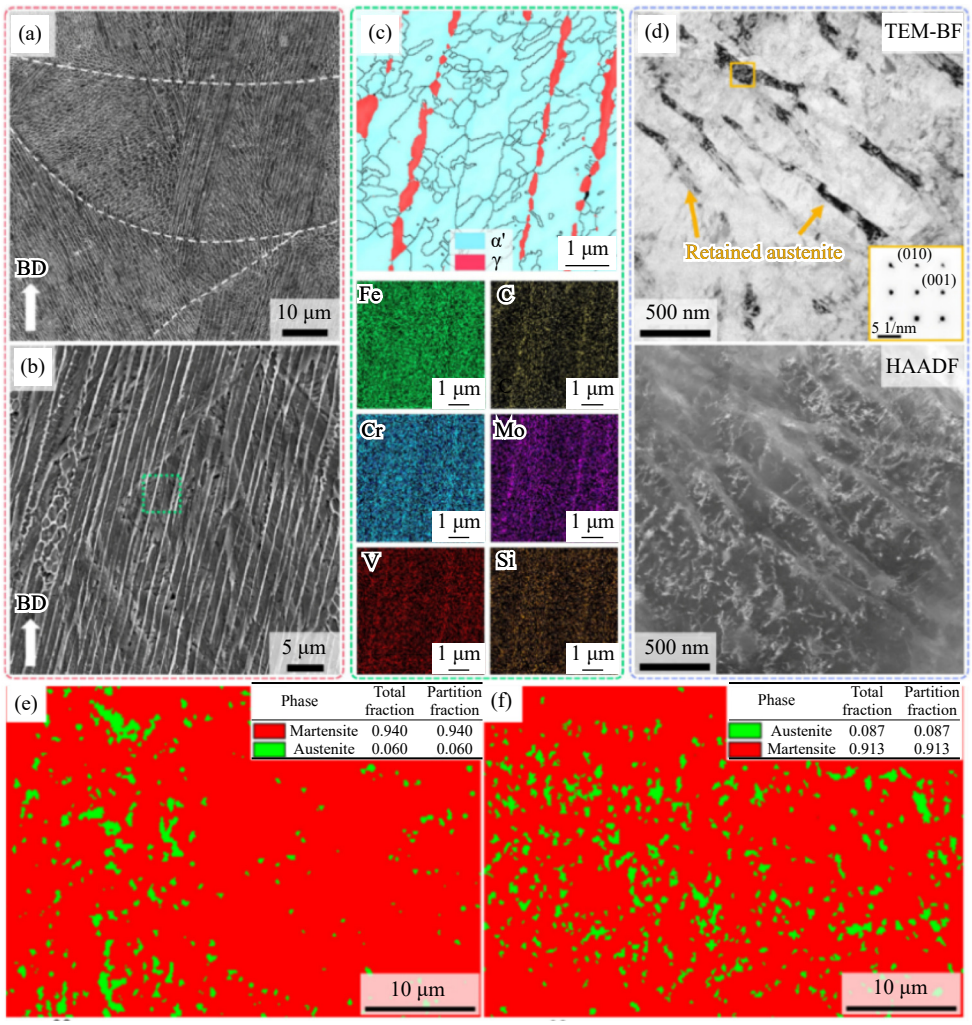

Fig. 4. (a–b) Microstructure, (c) phase map and corresponding EDS maps, (d) TEM bright-field (upper) and high angle annular dark field scanning-TEM micrographs viewed along the $[100]_\gamma$, with the inset showing the SAED pattern of the marked area of LPBF-processed H13 steel. Reprinted from *Scripta Mater.*, 214, Q.Y. Tan, Y. Yin, F. Wang, *et al.*, Rationalization of brittleness and anisotropic mechanical properties of H13 steel fabricated by selective laser melting, 114645, Copyright 2022, with permission from Elsevier; EBSD phase maps of the LPBF-processed H13 steel in (e) horizontal direction and (f) building direction [46].

martensite block, and several groups of martensite blocks with the same habit plane constitute a martensite packet. The minimum misorientation angle between different blocks is 10.53°. The grain boundaries (≥15°) identified in the EBSD map correspond to the martensite block boundaries [11,52]. The LPBF-processed H13 steel has a high fraction of high-angle grain boundaries (HAGBs) in both the horizontal and vertical sections, which also indicates a high volume fraction of martensite formed in LPBF-processed H13 steel [46,53]. Only the small volume fraction of retained austenite with the original orientation exhibited a weak texture in LPBF-processed H13 steel. Another reason is related to the scanning strategy. The rotation of the scanning direction induced a variation in the heat flux, which wrecked the epitaxial columnar structure [51–52].

3.1.3. Substructure in grains and nanoprecipitations

The substructures along the vertical plane exhibited a cellular and dendritic morphology, while the substructures in the horizontal direction predominantly exhibited a cellular structure, as shown in Fig. 6. The majority of studies regrade cellular substructures as distinct features in LPBF-processed materials, which are associated with constitutional supercooling and interfacial stability theory [54]. Prashanth *et al.* [55] explored the metastable cellular structure in LPBF-processed Al–12Si, AlSi10Mg, CrCoMo, and 316 LSS alloys and ascribed it to surface tension-driven instability. The region of metastable cellular substructure is full of elements rather than a specific phase in the above alloys, however, for the LPBF-processed H13 steel, the core of the cellular is the martensite and the cellular boundary is austenite, the formation mechanism of the cellular substructure is probably different from the 316 LSS steel. Krell *et al.* [43] first proposed the cellular substructure formation mechanism in H13 steel and thought it was related to elemental segregation. The high elemental concentration hinders martensite transformation, resulting in the retention of austenite. As shown in Fig. 6(f), the cellular walls were enriched in C, Cr, Mo, V, and Si. This region kept the retained austenite while the core of the cellular transformed into martensite. The characteristics of the LPBF process and the martensite transformation contributed to the formation of a special cellular substructure in LPBF-processed H13 steel. In addition, the high cooling rate pro-

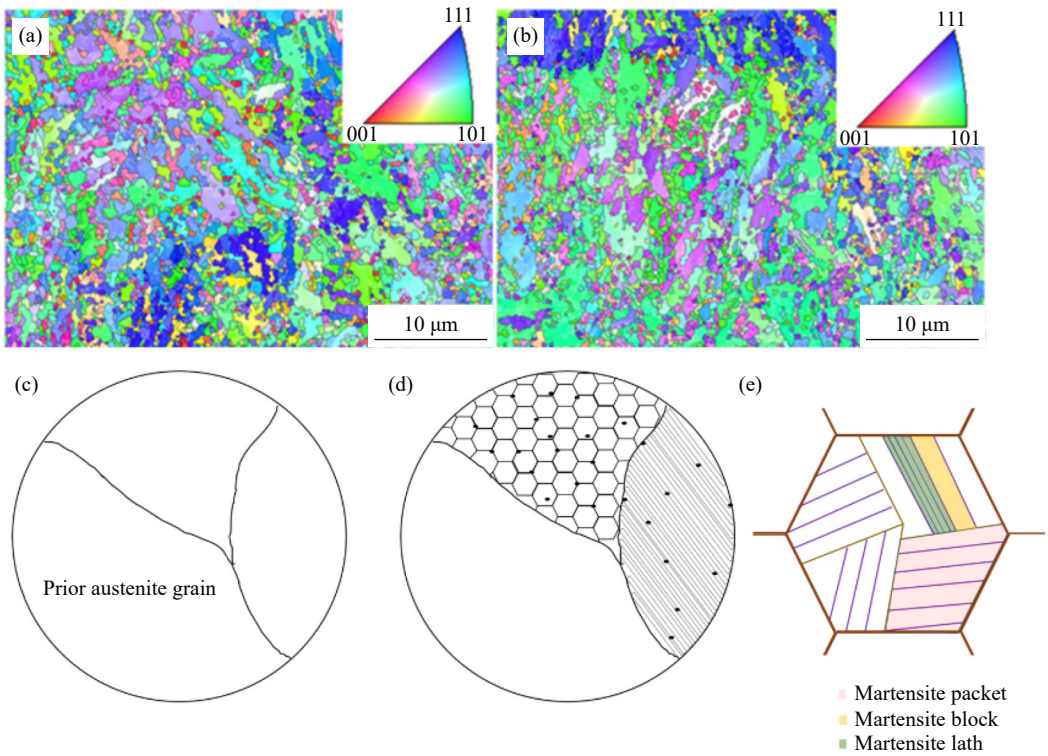

Fig. 5. EBSD IPF maps of the LPBF-processed H13 steel: (a) horizontal direction; (b) building direction [46]; (c) schematic diagrams of prior austenite grain structures; (d) microstructure after martensite transformation of LPBF2-processed H13 steel; (e) microscopic structure of martensite.

hibited carbon diffusion, which not only caused the higher content of retained austenite but also hindered the formation of carbides. Lee *et al*. [56] combined APT and TEM to detect fine MC (V-rich) and M_2C (Mo-rich) carbides. The volume fraction and size of carbides in the as-built H13 steel are determined by the effect of intrinsic HT. As shown in Fig. 6(b)–(e), the carbides could hardly be seen at the last melted layer, and there existed a few carbides in the bottom fusion zone. In the heat-affected zones, not only did the volume fraction of carbides increase but the cellular substructure was also partially dissolved. Furthermore, the intrinsic HT led to a decrease in hardness, primarily attributed to the diminished strength of the martensite phase resulting from carbide precipitation [9].

The main strengthening mechanism of conventional manufactured H13 steel is carbide precipitation strengthening, especially for high-temperature mechanical properties. Compared to the conventional manufactured H13 steel, the retained austenite and a lower volume fraction of carbides decreased the hardness and strength of the LPBF-processed H13 steel. It is necessary to control carbide precipitates, whether through intrinsic HT or post-treatment. The effect of intrinsic HT could be adjusted by changing the process parameters. For instance, the smaller the hatch spacing and layer thickness are, the larger the overlap between adjacent tracks and the intrinsic-HT effect [9]. The post-treatment is also an effective method to adjust carbides, as shown in Fig. 7, which can be divided into three types: (1) solution and tempering treatment, (2) direct tempering treatment, and (3) cryogenic and tempering treatment. The solution treatment eliminated the solidification characteristic structure and obtained a uniform distribution of elements through the diffusion of elements at high temperatures. Then, tempering the quenched sample induced the precipitation of a large number of carbides that were evenly distributed in the grains [45]. The microstructure of LPBF-processed H13 steel after solution and aging treatment is similar to that of conventional manufactured H13 steel with solution and aging treatment; however, this approach eliminates the cellular substructure. Direct tempering offers a method to eliminate the residual austenite and induce carbide precipitates without destroying the cellular substructure. Fig. 7(e) displays the microstructure of LPBF-processed H13 steel after tempering at 600°C for 1 h, with an enlarged view of carbides in the top right corner. The cellular substructures within grains underwent partial dissolution, resulting in a reduction in the volume fraction of retained austenite and the formation of nanoscale $M_{23}C_6$ carbides at the boundaries. However, after tempering at 700°C for 1 h, as depicted in Fig. 7(f), the cellular substructures were completely dissolved, leading to a further reduction in the content of the retained austenite and the formation of a high number density of coarse $M_{23}C_6$ precipitates [57]. During the tempering process, several microstructural changes occur, including the transformation of retained austenite to martensite, precipitation of carbides, dissolution of cellular substructures, and reduction in dislocation density. The formation of martensite and carbides increased the strength, while the dissolution of cellular substructures and reduction in dislocation density had the opposite effect, leading to decreased strength. Therefore, an optimal tempering

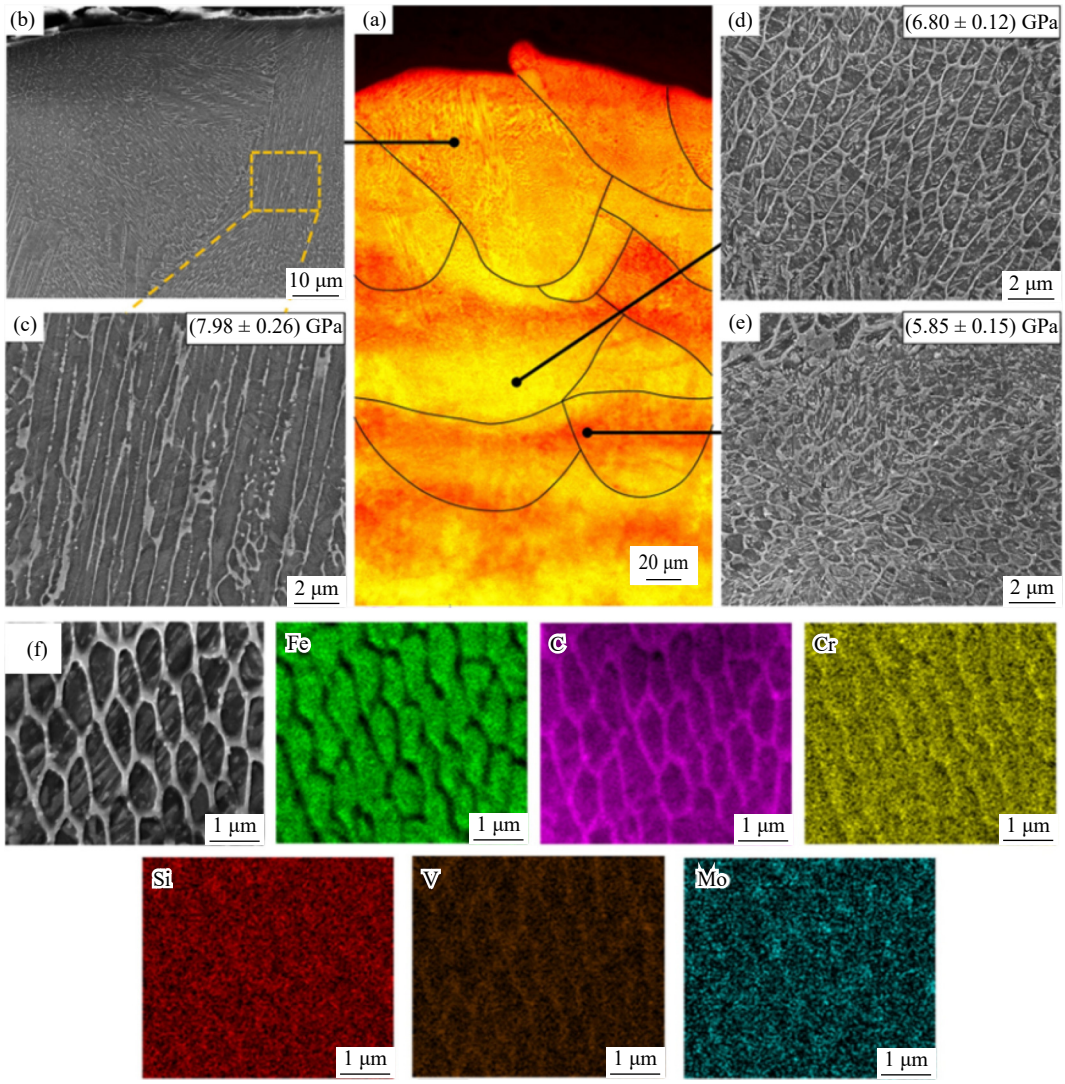

Fig. 6. (a) Schematic of the last melted layer, (b, c) microstructures of the last melted layer, (d) bottom fusion zone, (e) heat-affected zone of the LPBF-processed H13 steel in the vertical plane, and (f) substructures in the horizontal plane. Reprinted from *Addit. Manuf.*, 34, E.B. Fonseca, A.H.G. Gabriel, L.C. Araújo, P.L.L. Santos, K.N. Campo, and E.S.N. Lopes, Assessment of laser power and scan speed influence on microstructural features and consolidation of AISI H13 tool steel processed by additive manufacturing, 101250, Copyright 2020, with permission from Elsevier.

temperature and time combination is necessary to achieve the desired mechanical properties [57–58]. Another posttreatment that promotes carbide precipitation while preserving the cellular structure is cryogenic and low temperature treatment, as shown in Fig. 7(h)–(i), where the carbides are marked by a red arrow. Cryogenic treatment promoted the precipitation of carbon atoms and refined the martensite. Subsequently, during the low-temperature tempering treatment, the carbon atoms combined with other alloying elements to form carbides [59].

3.2. Maraging tool steels (18Ni300 tool steel)

3.2.1. Densification and meso-structure

Compared to H13 steel, the high content of Ni and low content of carbon enable maraging steels to have ductile martensite; therefore, adjusting the process parameters, such as the laser powder, scanning speed, and layer thickness, could obtain parts with a relative density higher than 99% [12,60–63]. Remelting could evidently reduce the large-sized pores at the expense of increased numbers of gas and keyhole pores [62]. The porosity of the vertically printed bars was less than that of the horizontally printed bars [63]. Suzuki *et al.* [61] utilized the deposited energy density to clarify the change in relative density and found that the relative density increased with increasing $Pv^{-1/2}$. When $Pv^{-1/2}$ reached approximately 3.3 $W \cdot mm^{-1/2} \cdot s^{1/2}$, the relative density became almost 100%. It can be seen from Fig. 8 that the deposited energy density could better represent the effects of the laser parameters on the relative density of LPBF-processed 18Ni300 steel compared to the volumetric energy density. The meso-structure of the horizontal plane and vertical plane of the LPBF-processed 18Ni300 steel did not show the alternating dark and bright layers, similar to the LPBF-processed H13 steel, which may indicate a weak intrinsic HT effect. The horizontal plane reveals the motion tracks of the laser beam. The molten pools with semielliptical shapes were approximately 50–100 μm high and approximately 50 μm wide on the vertical plane [64]. The semielliptical shape of

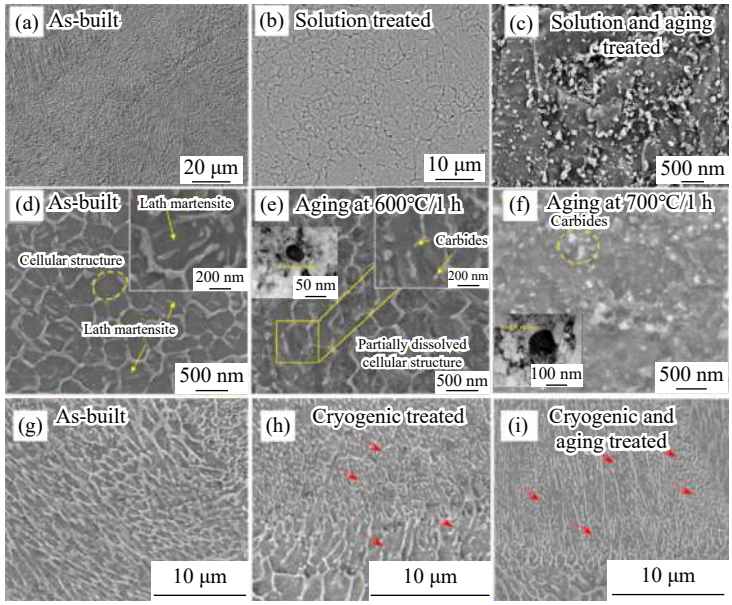

Fig. 7. Microstructure of (a, d, g) as-built, (b) after solution treatment at 1020°C/15 min, (c) after solution and at 650°C aging treatment. Reprinted from *Mater. Sci. Eng. A*, 753, F. Deirmina, N. Peghini, B. AlMangour, D. Grzesiak, and M. Pellizzari, Heat treatment and properties of a hot work tool steel fabricated by additive manufacturing, 109, Copyright 2019, with permission from Elsevier; after directing aging treatment at (e) 600°C and (f) 700°C for 1 h [57], (h) after at −196°C for 24 h cryogenic treatment, and (i) after cryogenic treatment and at 200°C for 2 h tempering treatment [59].

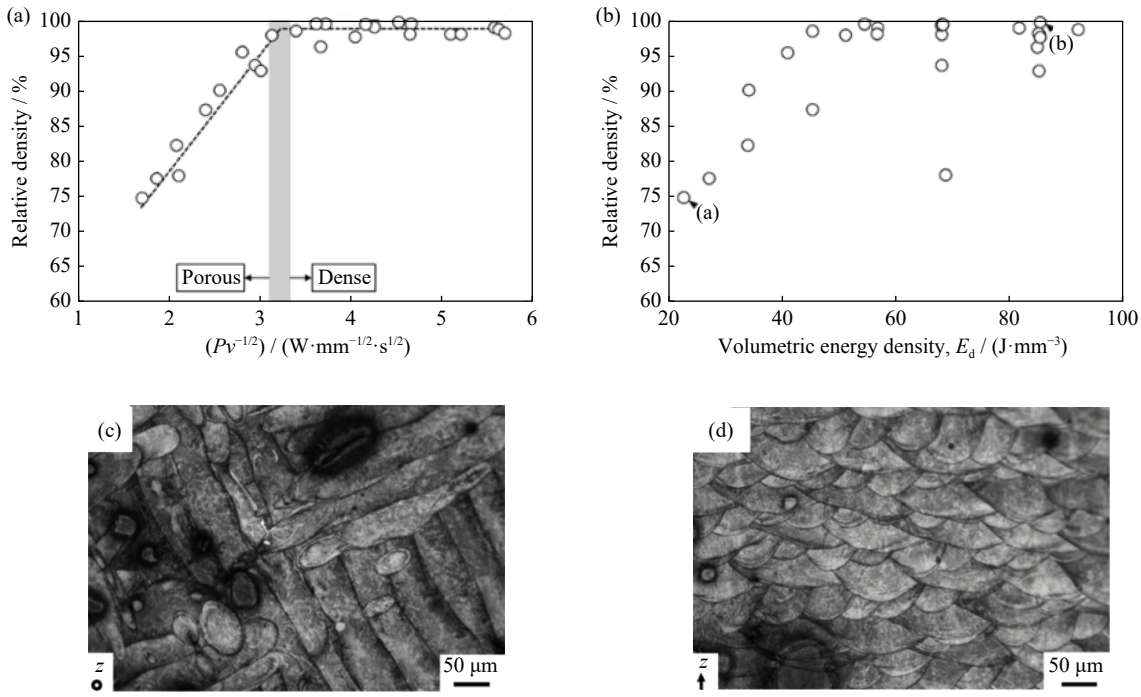

Fig. 8. Relative density as a function of (a) $Pv^{-1/2}$ and (b) volumetric energy density in LPBF-processed 18Ni300 steel. Reprinted from *Addit. Manuf.*, 28, A. Suzuki, R. Nishida, N. Takata, M. Kobashi, and M. Kato, Design of laser parameters for selectively laser melted maraging steel based on deposited energy density, 160, Copyright 2019, with permission from Elsevier; meso-structure of LPBF-processed 18Ni300 steel (c) in the horizontal plane and (d) vertical plane [64].

molten pools was related to the characteristics of the Gaussian laser heat source used in the LPBF process. The size of molten pools is related to the applied laser energy input. Compared with the LPBF process, the higher energy input of the directed energy deposition (DED) process led to the formation of a larger molten pool [12].

3.2.2. Microstructure

The phase constitution of the LPBF-processed 18Ni300 steel was found to consist of both martensite and austenite, similar to the LPBF-processed H13 steel [65]. This is in contrast to the conventionally produced 18Ni300 steel, which was fully martensitic [3]. Retained austenite was observed in both the intercellular and interdendritic regions. The formation mechanism is analogous to that of retained austenite in H13 steel. The phase transformation mechanism of martensitic steel is illustrated in Fig. 9(a)–(c). Upon cooling, the mol-

ten pool initially solidifies into the γ phase. Subsequently, the austenite transforms into martensite with a specific orientation relation as the temperature continues to decrease to the martensitic transformation temperature [64]. During solidification, the rapid cooling rate leads to the uneven distribution of elements. Consequently, elements with low melting points or low diffusion rates, such as Ti and Mo, are enriched in the intercellular and interdendritic regions [3,12,66]. These elements stabilize the austenite and effectively reduce the martensite transformation temperature [48]. As a result, the LPBF-processed 18Ni300 steels have a significant austenite content. The volume fraction and thermal stability of the retained austenite have an impact on the mechanical properties of 18Ni300 steel, and they can be adjusted through post-treatment [67]. As shown in Fig. 9(d)–(f), the reversion of martensite to austenite increased the quantity of austenite during direct aging treatment. The austenite nearly disappeared after the solution and aging treatment or the high-temperature aging treatment. The solution treatment eliminates elemental segregation and leads to the disappearance of preferential nucleation and growth sites for martensite during subsequent aging processes [68]. The direct aging temperature, as depicted in Fig. 9(g)–(i), affects the quantity and thermal stability of austenite. Increasing the aging temperature led to a higher volume fraction of martensite transforming into austenite while also promoting more austenite-to-martensite transformation during the cooling process. As the aging temperature increased, the required Ni partitioning for martensite-to-austenite reversion decreased, resulting in enhanced formation of austenite. Concurrently, the stabilizing elements were uniformly distributed, leading to a decrease in the thermal stability of austenite [67].

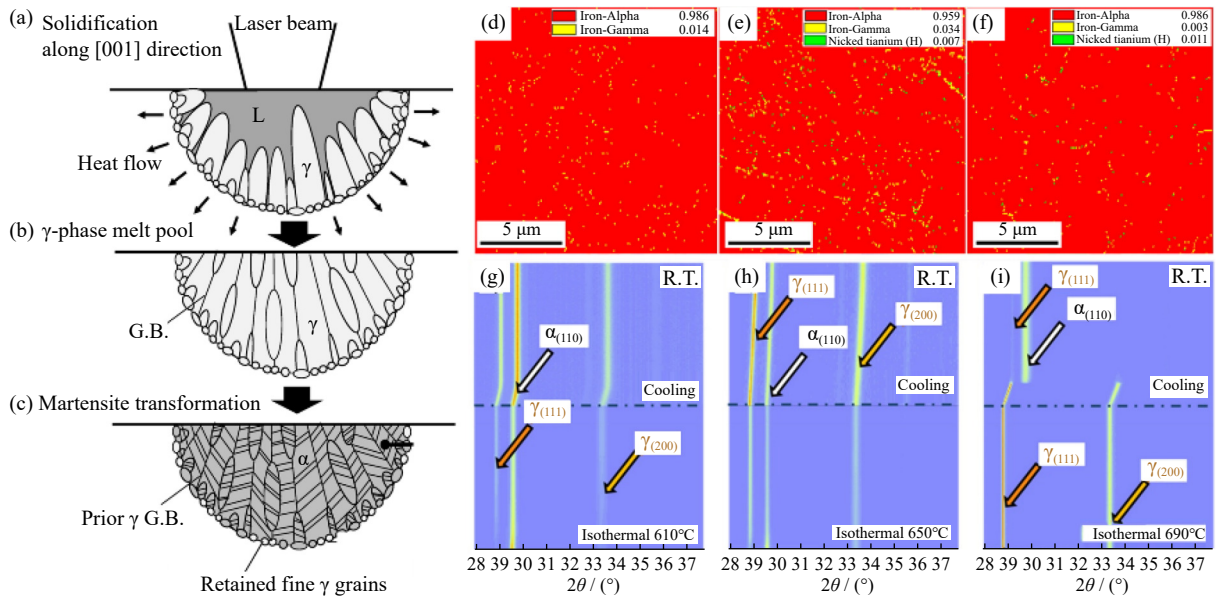

Fig. 9. (a–c) Schematics of the phase transformation process in the 18Ni300 steel [64]; EBSD phase map of (d) as-built, (e) after direct aging, and (f) solution and aging treatment of LPBF-processed 18Ni300 steel. Reprinted from *Mater. Des.*, 139, J. Mutua, S. Nakata, T. Onda, and Z.C. Chen, Optimization of selective laser melting parameters and influence of post heat treatment on microstructure and mechanical properties of maraging steel, 486, Copyright 2018, with permission from Elsevier; time-resolved synchrotron X-ray diffraction characterization (XRD) during the simulation of inter-critical tempering cycles at (g) 610°C, (h) 650°C, and (i) 690°C of 18Ni300 steel. Reprinted from *Addit. Manuf.*, 29, F. Conde, J. Escobar, J. Oliveira, A. Jardini, W.B. Filho, and J. Avila, Austenite reversion kinetics and stability during tempering of an additively manufactured maraging 300 steel, 100804, Copyright 2019, with permission from Elsevier (R.T. means room temperature and G.B. means grain boundary).

The LPBF-processed 18Ni300 steel does not exhibit a pronounced crystallographic texture [68–69]. Fig. 10(a) illustrates the random grain orientations and the formation of numerous small grains in the vertical section [68]. Fig. 10(b) shows that the central molten pool of the as-built 18Ni300 on the horizontal section displays a significant presence of fine grains, exhibiting an epitaxial growth pattern perpendicular to the scanning direction [69]. As described above, the martensite transformation induced prior austenite containing several martensite blocks with different grain orientations. In addition, many researchers thought the weak texture in LPBF-processed 18Ni300 steel was attributed to the laser rotation during deposition of new layers, which altered the heat flow conditions and consequently the crystal growth direction [66–69]. It is worth noting that the as-built 18Ni300 steel had a higher fraction of low-angle grain boundaries (LABs, 2°–15°) [65,68]. The high-volume fraction of LABs may indicate a large number of substructures. The volume fraction of LABs increased after the aging treatment due to the hindrance of dislocation movement by the precipitated phase. The high-temperature solution treatment facilitated grain growth, resulting in a high volume fraction of HABs [65].

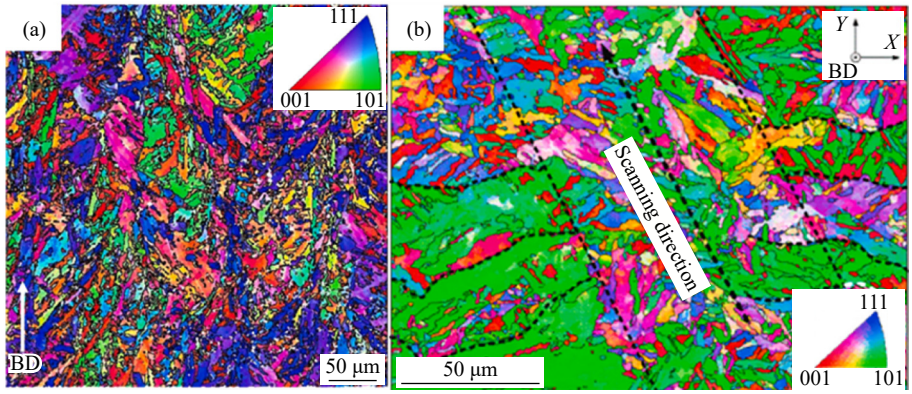

Fig. 10. EBSD IPF maps in the (a) vertical plane. Reprinted from *Mater. Sci. Eng. A*, 854, J. Song, Q, Tang, H. Chen, *et al.*, Laser powder bed fusion of high-strength maraging steel with concurrently enhanced strength and ductility after heat treatments, 143818, Copyright 2022, with permission from Elsevier, and (b) horizontal plane of LPBF-processed 18Ni300 steel. Reprinted from *Mater. Sci. Eng. A*, 830, Z.F. Mao, X.D. Lu, H.R. Yang, X.D. Niu, L.J. Zhang, and X.F. Xie, Processing optimization, microstructure, mechanical properties and nanoprecipitation behavior of 18Ni300 maraging steel in selective laser melting, 142334, Copyright 2022, with permission from Elsevier.

3.2.3. Substructure in grains and nanoprecipitations

On the horizontal section of the as-built LPBF-processed 18Ni300 steel, as shown in Fig. 11(a), submicron-sized hexagonal cellular grains were uniformly distributed in the middle range of the laser track, while elongated acicular grains were distributed in the margin region [12–13,69–70]. The formation mechanism is associated with the heat flux from the center to the edge, resulting from the Gaussian distribution of laser energy, as depicted in Fig. 11(b) [13,69]. Bodziak *et al.* [71] proposed that the microstructure at the border of tracks was influenced by the intrinsic thermal effect. As a new layer is built, the already solidified grains of the previous layer receive enough energy to generate recrystallization and growth. The vertical cross-section reveals the presence of columnar dendritic substructures at the bottom of the molten pool, cellular substructures in the middle, and coarse equiaxial grains at the inter-pool boundary. The variation in substructures was associated with the depth-wise change in the temperature gradient to solidification rate ratio (G/R) within the molten pool [13]. Other studies only revealed the cellular substructures and corresponding epitaxial growth in the vertical plane, suggesting limited time for elemental diffusion to generate secondary dendrite arms [64,66,68,70]. As described above, the substructures of the 18Ni300 steel were composed of dendrites and cellular structures, which are similar to those of the H13 steel. These typical substructures were related to the special process characteristics of the LPBF process, such as high cooling rates, constitutional supercooling, solute segregation, Marangoni convection, and fast solidification rates [67,72].

There is a divergence of opinions regarding the formation of nanoprecipitates in LPBF-processed 18Ni300 steel. Some

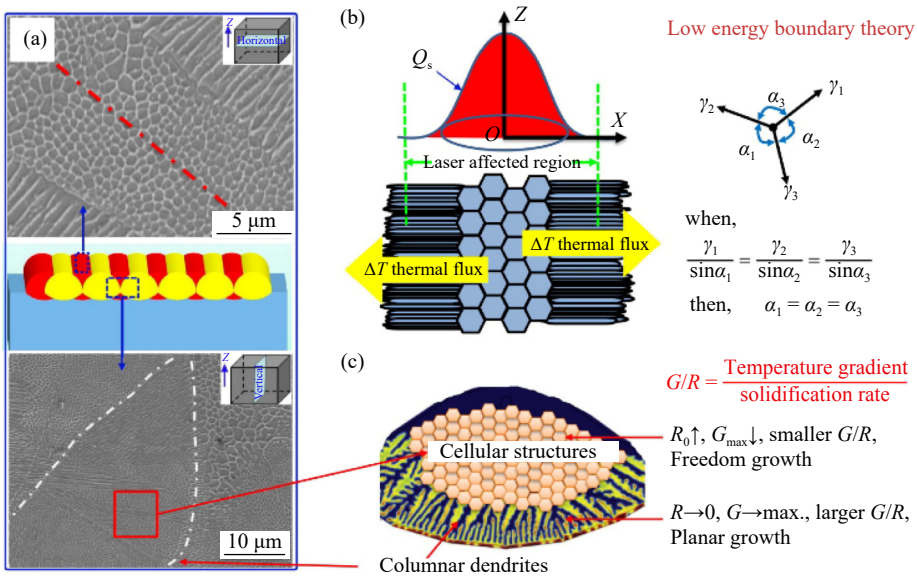

Fig. 11. (a) Substructures and (b–c) schematics of the formation mechanism of substructures in LPBF-processed18Ni300 steel in the vertical and horizontal planes. Reprinted from *Mater. Des.*, 830, C.L. Tan, K.S. Zhou, W.Y. Ma, P.P. Zhang, M. Liu, and T.C. Kuang, Microstructural evolution, nanoprecipitation behavior and mechanical properties of selective laser melted high-performance grade 300 maraging steel, 23, Copyright 2017, with permission from Elsevier.

research indicates the presence of nanoprecipitates in as-built parts induced by the intrinsic-HT effect [73]. Mao *et al*. [69] found nanoprecipitates and amorphous nanocrystals by TEM. Fig. 12 (a)–(b) illustrates the needle-shaped, uniformly distributed Ni_3(Mo, Ti) nano-sized intermetallic phases on the columnar martensite matrix [13]. Other researchers believed that no precipitates or elemental clusters were formed in the as-built 18Ni300 steel [71,74]. Fig. 12(c)–(d) illustrates the absence of precipitates (clusters) in the LPBF-processed 18Ni300 steel. Ti–Ti clusters were observed in the laser metal deposition (LMD)-processed 18Ni300 steel, which was attributed to the high intrinsic-HT effect of LMD [3]. In comparison to the LMD process, the higher scanning speed and smaller molten pool in the LPBF process result in a less significant intrinsic-HT effect. The effect of intrinsic HT can be adjusted by changing the process parameters; for example, laser remelting causes solidified tracks and layers to undergo more reheating cycles and increases the formation of nanoprecipitates [62]. In conventionally produced 18Ni300 steel, solution and aging heat treatments are used to adjust the size and volume fraction of precipitates to improve the precipitation strengthening effect, which is the same for LPBF-processed 18Ni300 steel [3]. After solution treatment, the microstructure is fully martensite without precipitate formation. The aging treatment further induces the formation of uniform nanoprecipitations [70]. Direct aging directly induces the formation of precipitates at the basis of not destroying the solidification microstructure. The effect of aging time on the microstructure was less than that of aging temperature [72]. The same precipitated phases can be obtained at a higher aging temperature with a shorter aging time. For example, after aging at 480°C for 5 h, three different types of precipitates were precipitated in the matrix, namely, Ni_3Ti, $(Fe, Ni, Co)_3(Mo, Ti)$, and Fe_7Mo_6 [74]. After direct aging at 510°C for 2 h, the type of Ni_3Ti precipitates included $(Fe, Ni, Co)_3(Ti, Mo)$ and $Ni_3(Ti, Mo)$ with spherical shapes and plate-like shapes, respectively, and the spherical precipitation enriched in Mo of Fe_7Mo_6 formed [71]. If the intrinsic-HT effect could facilitate the formation of precipitates in both H13 steel and 18Ni300 steel, it would eliminate the need for post-heat treatment, resulting in cost reduction [14]. Hence, exploring the utilization of the intrinsic-HT effect to control precipitates is imperative.

4. The mechanical and thermal properties of LPBF-processed tool steels

4.1. Tensile property

4.1.1. Carbon tool steels (H13 tool steel)

Due to the challenges associated with fabricating H13 tool steel using the LPBF process, researchers have been exploring various process parameters in an attempt to achieve fully

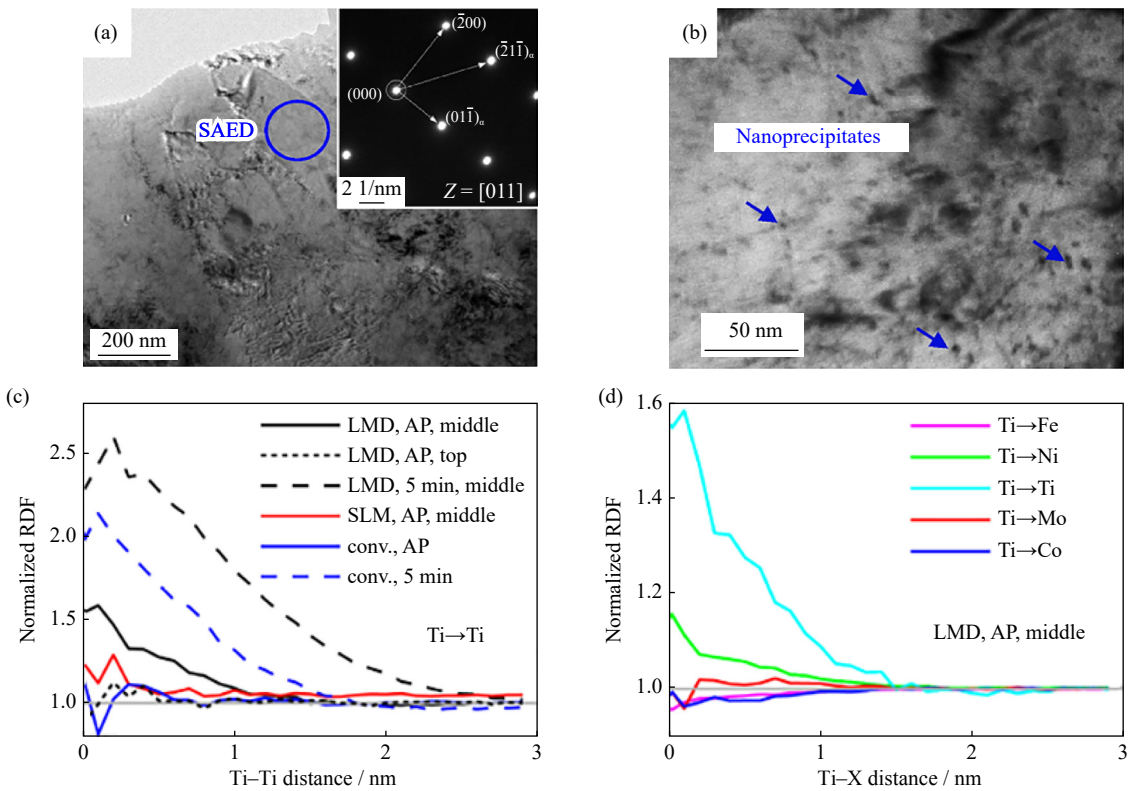

Fig. 12. TEM bright-field images of (a) columnar martensite with the corresponding SAED pattern and (b) nanoprecipitates of LPBF-processed 18Ni300 steel. Reprinted from *Mater. Des.*, 830, C.L. Tan, K.S. Zhou, W.Y. Ma, P.P. Zhang, M. Liu, and T.C. Kuang, Microstructural evolution, nanoprecipitation behavior and mechanical properties of selective laser melted high-performance grade 300 maraging steel, 23, Copyright 2017, with permission from Elsevier, (c) Ti–Ti radial distribution functions (RDFs) for different manufacturing processes, and (d) various RDFs (Ti as center atom and Fe, Ni, Ti, Mo, and Co as target atoms) of LMD-processed 18Ni300 steel [3].

dense H13 steel. We summarized the process conditions, microstructures, and mechanical properties of H13 steel fabricated by the LPBF process, as presented in Table 1. Significant variations in the microstructure and performance under different process parameters and subsequent treatment conditions can be observed. To provide a clear and comprehensive comparison of the LPBF-processed H13 steel tensile properties, the tensile strength and strain of H13 steel produced at various process parameters are presented in Fig. 13. The as-built tensile properties of LPBF-processed H13 steel exhibit a wide dispersion, with tensile strengths ranging from 1220 to 2000 MPa and tensile strains varying from 0.35% to 12.4%. The high density of defects has a significant impact on the tensile performance. For example, the lack of fusion defects generated by low-volume energy density and the small-sized gas pores and keyhole-type pores generated by high-volume energy density lead to premature fracture of the alloys [56]. The LPBF-processed H13 steel with optimal process parameters has similar tensile properties as the conventional manufactured H13 steel, even having a slightly higher strength and plasticity than the conventional processed H13 steel. In addition, the post-treatment could further improve the tensile properties. The high cooling rate leads to the formation of a finer grain size and higher dislocation density in the martensite phase of LPBF-processed H13 steel compared to conventionally processed H13 steel. As a result, the LPBF-processed H13 steel exhibits enhanced strength due to the combined effects of dislocation strengthening and fine grain strengthening. Additionally, the cellular substructures serve as another significant strengthening mechanism [46]. The cellular substructures in 316SS steel triggered the steady strain-hardening ability at high stress levels. The regulatory effect of the cellular substructure makes it relatively stable under deformation and helps to retain dislocations [54]. The LPBF-processed H13 steel exhibits a typical two-phase microstructure, which imparts unique properties to the material, such as continuous yield and rapid initial work hardening [51]. However, the impact of retained austenite on the tensile

Table 1. Overview of published microstructural characteristics and mechanical properties of H13 carbon-bearing tool steel

Process condition	Microstructure	YS / MPa	UTS / MPa	Elongation / %	Hardness, HV	Refs.
Wrought H13 AP	α' + Ferrite	1569–1650	1930–1990	9–12	201 ± 2.2	[8,75]
Wrought H13 after SH	α' + K	1280–1290	—	13–15	708.1 ± 12.6	[75–76]
LPBF-H13 AP without PH	α' + γ	—	1909	12.4	561	[51]
LPBF-H13 AP without PH at 47.6 J/mm^3	α' + γ (0.6%) + K	1223 ± 30	1620 ± 25	4.7 ± 0.7	585	[52]
LPBF-H13 AP without PH at 71.4 J/mm^3	α' + γ (0.4%) + K	1473 ± 22	1850 ± 35	4.3 ± 0.8	602	
LPBF-H13 AP without PH at 100 J/mm^3	α' + γ (0.9%) + K	1540 ± 25	1920 ± 30	3.1 ± 0.6	615	
LPBF-H13 AP without PH at the optimized parameters	α' + γ (6%–8.7%) + K	1468 ± 27	1837 ± 23	8.5 ± 0.6	537.5	[46]
LPBF-H13 AP without PH at the optimized parameters	α' + γ (7.8%) + K	1342 ± 67	1704 ± 30	1.55 ± 0.05	585 ± 6	[56]
LPBF-H13 AP without PH	α' + γ (26.9%)	1245	1366	22	—	[15]
LPBF-H13 after SA without PH	α' + γ (1.66%) + K (7.38%)	1385	1613	8	—	
LPBF-H13 AP without PH	α' + γ	1236 ± 178	1712 ± 103	4.1 ± 1.2	894 ± 48	[44]
LPBF-H13 AP with 200°C PH	α' + γ (higher)	835 ± 23	1620 ± 215	4.1 ± 2.3	706 ± 147	
LPBF-H13 AP with 400°C PH	B (bainite)	1073 ± 72	1965 ± 145	3.7 ± 1.7	667 ± 83	
LPBF-H13 AP without PH	α' + γ	1190 ± 50	2005 ± 68	6.9 ± 0.5	—	[11]
LPBF-H13 AP with 100°C PH	α' + γ (15%)	1468 ± 23	1837 ± 27	8.5 ± 0.6	—	[57]
LPBF-H13 after DA 600°C/1 h with 100°C PH	α' + γ (8%) + K	1647 ± 29	2013 ± 35	4.1 ± 0.3	—	
LPBF-H13 after DA 700°C/1 h with 100°C PH	α' + γ (4%) + K (large amount and coarse)	887 ± 18	1083 ± 21	12.3 ± 1.2	—	
LPBF-H13 AP with 200°C PH	α' + γ + K	1155	1297	4.2 ± 3.0	428 ± 3.1	[77]
LPBF-H13 after SA with 200°C PH	α_T + γ + K (increased)	1447	1640	3.3 ± 1.6	511 ± 4.7	
LPBF-H13 after SA+HIT with 200°C PH	α_T + K (reduced porosity)	1502	1743	6.6 ± 0.6	562 ± 4.5	
LPBF-H13 AP with 180°C PH	α' + γ (19.1%) + less K	—	1847.5 ± 24.6	11.8 ± 0.4	—	[59]
LPBF-H13 after cryogenic treatment with 180°C PH	Finer α' + γ (15.7%) + small sized K	—	1889.1 ± 23.2	10.7 ± 0.4	—	
LPBF-H13 after cryogenic and tempering treatment with 180°C PH	α' + γ (14.2%) + denser K	—	1917.3 ± 25.2	19.3 ± 0.4	—	

Notes: AP—as produced, PH—preheating, SA—solution treated, SH—solution and aging heat treated, DA—direct aging treated, K—carbides, α'—martensite, γ—austenite, and α_T—tempering martensite.

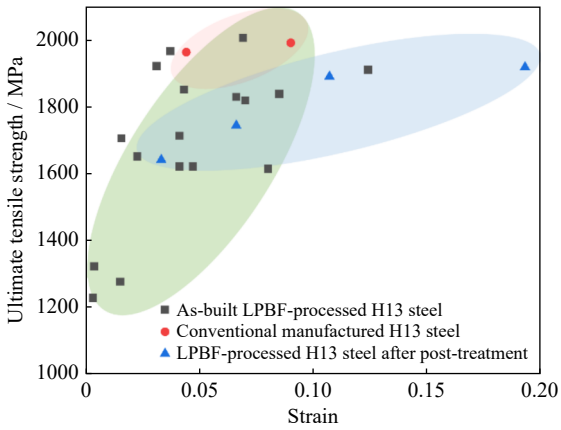

Fig. 13. Tensile properties of the conventionally manufactured and LPBF-processed H13 steel in the as-built state and after post-treatment state [11,15,44,46,49,51–52,56–57,77].

properties of LPBF-processed H13 steel is different. Fig. 14 (a)–(c) shows that the as-built H13 steel with a higher volume fraction of retained austenite had a higher ductility than the heat-treated H13 steel with a lower content of retained austenite. The volume fraction of the retained austenite decreased while the martensite content increased after tensile deformation [15]. Most researchers have attributed this phenomenon to the TRIP effect. During the tensile process, most deformation occurred in retained austenite and induced the TRIP effect, which absorbed the stress and prohibited the formation of cracks [46,49,56]. However, not all the retained austenite transformed to lath martensite enriched with dense dislocations. The type of transformed martensite was related to the content of carbon. The higher content of carbon induced the formation of twin-type martensite, which was det-

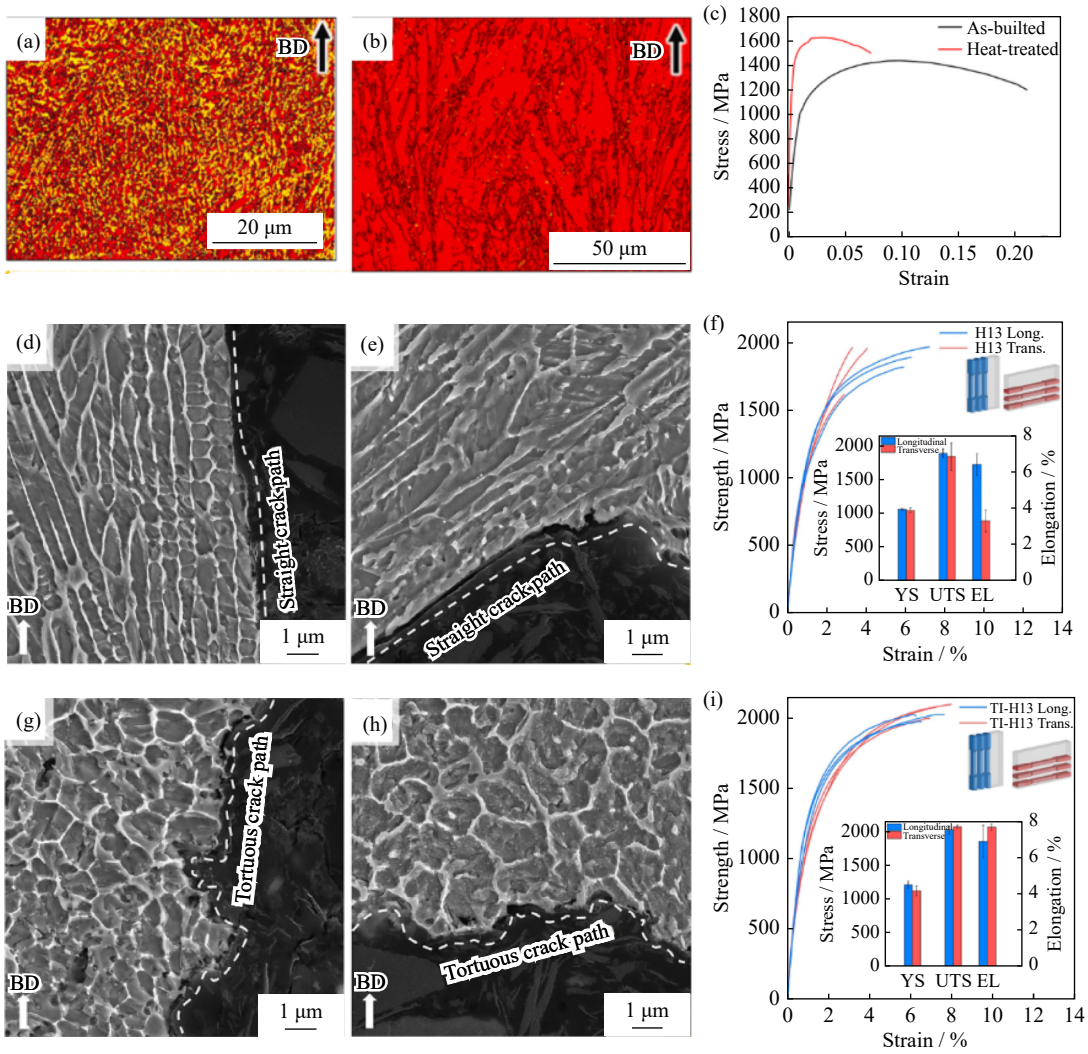

Fig. 14. EBSD phase maps of (a) as-built and (b) heat-treated before tensile test, (c) engineering stress strain curves of as-built and heat-treated LPBF-processed H13 tool steel. Reprinted from *Mater. Today Commun.*, 33, K. Chadha, Y. Tian, K. Nyamuchiwa, J. Spray, and C. Aranas Jr, Austenite transformation during deformation of additively manufactured H13 tool steel, 104332, Copyright 2022, with permission from Elsevier, (d–e) fracture surface of the LPBF-processed H13 steel and (g–h) the TiN-inoculated H13 steel after transverse loading and longitudinal loading, and the engineering tensile stress–strain curves of the LPBF-processed (f) H13 steel and (i) TiN-inoculated H13 steel. Reprinted from *Scripta Mater.*, 219, Q.Y. Tan, H.W. Chang, Y. Yin, *et al.*, Simultaneous enhancements of strength and ductility of a selective laser melted H13 steel through inoculation treatment, 114874, Copyright 2022, with permission from Elsevier.

rimental to the ductility of the H13 steel. Tan *et al.* found that the retained austenite transformed into the twin-type martensite and ω-Fe phase during deformation. The twin-type martensite had a higher susceptibility to fracture due to the large lattice distortion, and the ω-Fe phase impeded the motion of twins [11]. Furthermore, the morphology of retained austenite plays a role in influencing the tensile properties. Analysis of fracture surfaces in tensile samples revealed that cracks propagated along the elongated retained austenite boundaries, which acted as weak regions to facilitate crack propagation [11]. Fig. 14(d)–(f) shows that the as-built H13 steel had high ductility and strength along the longitudinal direction compared to the transverse direction. The elongated retained austenite films along the longitudinal acted as load-bearing faces upon the transverse loading condition. After heterogeneous treatment to refine the austenite grains, as shown in Fig. 14(g)–(i), the crack propagation path becomes more tortuous, and the plasticity of the alloy is improved [53].

4.1.2. Maraging steels (18Ni300 tool steel)

As previously mentioned, 18Ni300 steel with full density is more processable in the LPBF process than H13 steel. Therefore, the tensile property of LPBF-processed 18Ni300 steel with full density shows a relatively uniform tensile property. Similarly, the process conditions, microstructural characteristics, and mechanical properties of 18Ni300 fabricated by the LPBF process are summarized in Table 2. In comparison to the LPBF-processed H13 steel with a high content of carbon, the high content of alloying elements in 18Ni300 steel improves ductility but reduces strength. Likewise, the yield and ultimate strength of the LPBF-processed 18Ni300 steel are nearly equal to or slightly higher than those of the conventional manufactured 18Ni300 steel in the non-aged state [66,69,80]. The main strengthening mechanisms of the LPBF-processed 18Ni300 included grain strengthening, high dislocation density strengthening, nanoprecipitation strengthening, and cellular substructure strengthening, which was the same as the H13 steel [65,80–81]. The effect of the austenite on the tensile property in LPBF-processed 18Ni300 steel is different from that in the LPBF-processed H13 steel. As shown in Fig. 15(a)–(b), the austenite located at the boundaries did not effectively impede crack propagation, and the austenite went through serious deformation. In addition, the effect of the austenite on the tensile property is smaller than the effect of the precipitation strengthening. Fig. 15(c) depicted the aged sample with a high-volume fraction of austenite had worse ductility and better strength than the as-built sample, which was related to the precipitates formed during the aging process [82]. Fig. 15(d) summarizes the tensile properties of 18Ni300 steel with different manufacturing processes and post-treatments, revealing that the post-treatment significantly enhances strength while reducing plasticity. In the LPBF-processed 18Ni300 steel, the specimens with the building direction vertical to the loading direction had slightly higher tensile strength and much higher elongation compared to the specimens with the building direction paral-

Table 2. Overview of published microstructure characteristics and mechanical properties of 18Ni300 Maraging tool steel

Process condition	Microstructure	YS / MPa	UTS / MPa	Elongation / %	Hardness, HV/HRC	Refs.
Wrought 18Ni300 after solution	α'	760–895	830–1170	6–17	30–37 HRC	[8,78]
Wrought 18Ni300 after SA	α' + intermetallic	1790–2070	1830–2100	5–11	525 HV/54 HRC	
LPBF-18Ni300 AP	α' + γ (1.4%)	—	11125	10.38	330–403	[65]
LPBF-18Ni300 after DA	α' + γ (3.4%) + intermetallic (0.7%)	—	—	—	610	
LPBF-18Ni300 after SA	α' + intermetallic (1.1%)	—	2033	5.27	618	
LPBF-18Ni300 AP	α' + γ	1030 ± 17	1084 ± 15	10.5 ± 0.8	345 ± 10	[62]
LPBF-18Ni300 AP with optimal remelting process	α' + γ + nanoprecipitates	1022 ± 8	1083 ± 13	13 ± 3.5	362 ± 4	
LPBF-18Ni300 AP	α' + γ	—	1159.7	6.2	428.2	[79]
LPBF-18Ni300 after solution	α'	—	1028.1	15.4	366.5	
LPBF-18Ni300 after SA	α' + precipitates	—	2009.5	14.1	711.5	
LPBF-18Ni300 AP	Fine α'	1080	1205	12.0	~420	[78]
LPBF-18Ni300 after solution	Coarse α'	800	950	13.5	~330	
LPBF-18Ni300 after SA	Coarse α' + precipitates	1750	1800	5.1	~590	
LPBF-18Ni300 AP	α' + γ (small minority) + nanoprecipitates	1052 ± 20	1245 ± 3	10.5 ± 0.5	—	[69]
LPBF-18Ni300 after SA	α' + γ + more nanoprecipitates	1762 ± 24	1915 ± 22	5 ± 0.5	—	
LPBF-18Ni300 AP	α' + γ (11.38%)	914.9 ±12.5	1187.6 ± 10.4	6.14 ± 1.33	371	[82]
LPBF-18Ni300 after DA	α' + γ (17.17%)	1870.3 ± 53.8	1956.9 ± 54.2	2.07 ± 0.32	~570	
LPBF-18Ni300 AP	α' + γ (5.8%)	1214 ± 99	1290 ± 114	13.3 ± 1.9	39.9 ± 0.1 HRC	[81]
LPBF-18Ni300 after DA	α' + γ (9.4%)	1998 ± 32	2217 ± 73	1.6 ± 0.26	58 ± 0.1 HRC	
LPBF-18Ni300 AP	α' + γ	554.7 ± 13	1173.1 ± 68	10.9 ± 0.45	407.1 ± 10.6	[80]
LPBF-18Ni300 after DA	α' + γ (increase) + precipitates	2065 ± 65	2225 ± 51	4.2 ± 0.38	443.0 ± 6.2	

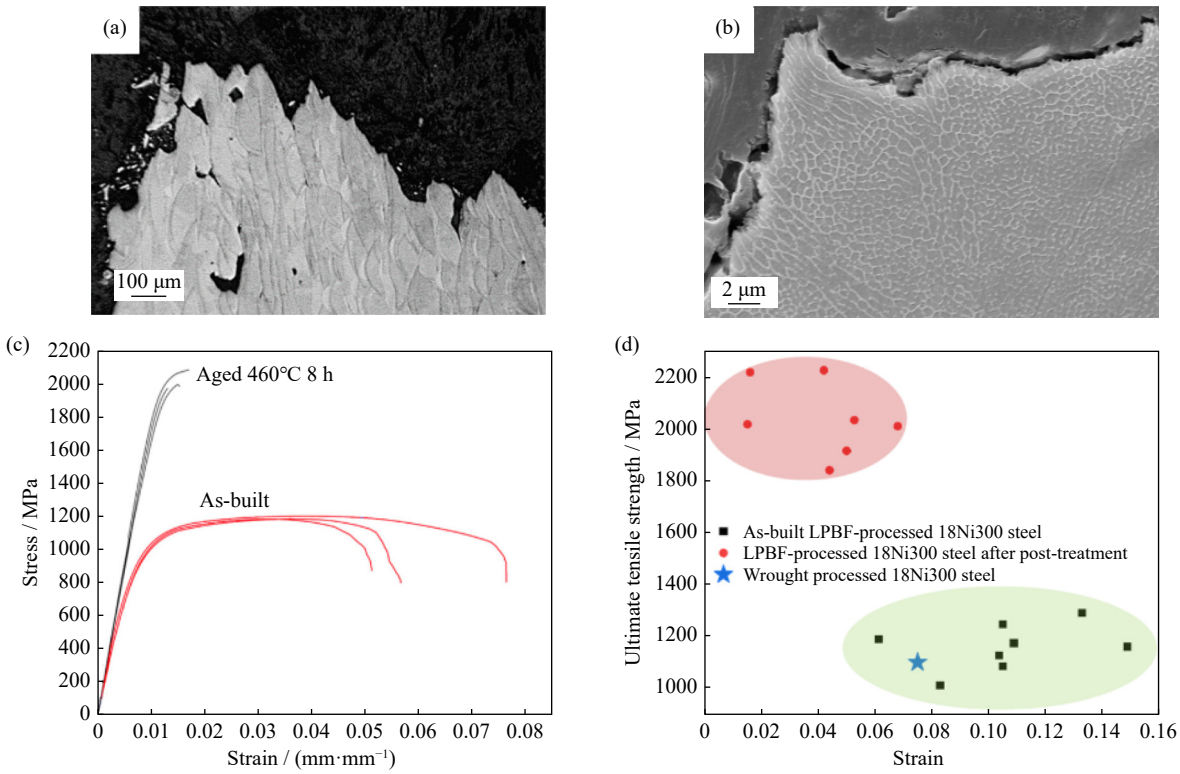

Fig. 15. Microstructure of the (a) as-built and (b) 460°C peak-aged LPBF-processed 18Ni300 steel after breaking, (c) tensile stress–strain curves of the as-built and peak-aged LPBF-processed 18Ni300 steel [78]; (d) tensile properties of the conventionally manufactured and LPBF-processed 18Ni300 steel in the as-built state and after post-treatment state [62,65,69,78–82].

lel to the loading direction. Mutua *et al*. [65] attributed the lower elongation to layer separation. Ong *et al*. [63] thought the mechanical anisotropy was related to the difference in porosity density. The post heat-treatment could eliminate the differences in microstructure and defects between samples deposited in different orientations [65,83].

The LPBF-processed H13 steel and 18Ni300 steel exhibit a two-phase microstructure. The strengthening mechanisms for the LPBF-processed 18Ni300 steel and LPBF-processed H13 steel are the same, including grain strengthening, dislocation strengthening, nanoprecipitation strengthening, and cellular strengthening. However, the different thermal stabilities and morphologies of the constituent phases contribute to different crack propagation and deformation behaviors. We conclude the deformation behavior of the LPBF-processed 18Ni300 steel and LPBF-processed H13 steel during the tensile test, as shown in Fig. 16. In the H13 steel, cracks propagate along the austenite boundary, and at the same time, the stress concentration in the crack tip may lead to the phase transformation. For the 18Ni300 steel, the austenite deformed substantially and cracked across the austenite, but no phase transformation occurred. It is evident that austenite plays a crucial role in the tensile properties of tool steels. By controlling the thermal stability and mechanical properties of retained austenite, such as altering the volume fraction and elemental composition, tensile properties can be improved.

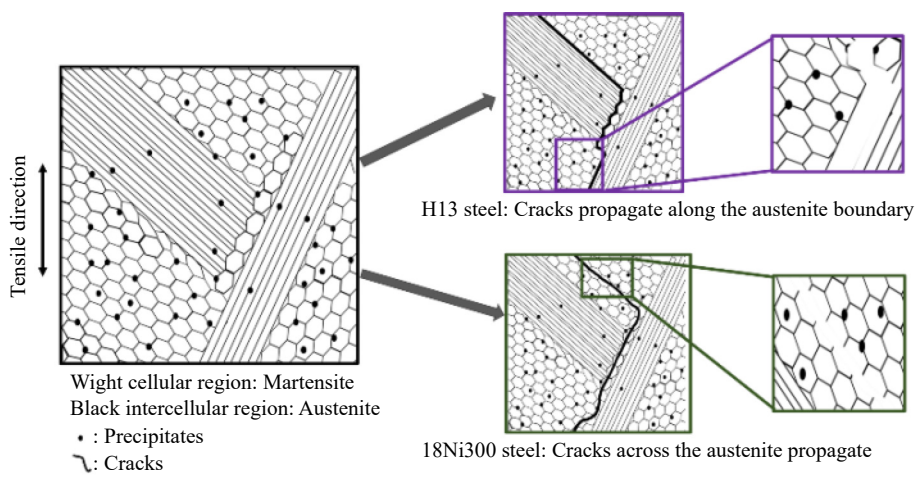

Fig. 16. Schematic of crack propagation and deformation behavior of the LPBF-processed H13 steel and LPBF-processed 18Ni300 steel.

4.2. Wear behavior

4.2.1. Carbon tool steels (H13 tool steel)

H13 steel has good high-temperature strength, ductility, fatigue properties, and low cost and is widely used to make molds, such as hot forging and press hardening [84]. During the service of these molds, they endured high temperature, high mechanical loads, and fatigue stress. In these applications, the main failure mechanism is wear [85]. It is necessary to explore the wear performance of H13 steel. Currently, the majority of research on wear performance is aimed at conventional H13 steel, and there is little information available on the wear performance of LPBF-processed H13 steel [8]. Increasing the hardness of conventionally produced H13 steel can significantly enhance the wear performance. Post-treatment is a widely used method to enhance the friction performance of alloys. However, the optimal post-treatment system may vary under specific wear conditions. For example, under high-pressure loads, samples with shorter tempering times exhibited better wear resistance. This is because the high localized pressure induced in-situ surface tempering, which led to the transformation of the martensite into a softer tempered martensite [86]. The oxidation performance of materials also plays an important role in the wear resistance under high-temperature wear conditions. The factors that control wear performance vary under different wear mechanisms. When the substrate strength was sufficient to withstand the tribo-oxide layer, the presence of the tribo-oxide layer led to a reduction in the wear rate. However, as the temperature increased, the strength of the softened substrate decreased, and it could no longer support the tribo-oxide layer. In this case, the controlling factors influencing the wear behavior shifted to the hardness and microstructural variation of the H13 steel [87]. The LPBF-processed H13 steel with fine microstructures and high strength may have good wear resistance. For LPBF-processed H13 steel, ground-and-polished H13 steel showed the lowest friction coefficient, followed by the as-printed state, while both polishing alone and laser-surface texturing increased the friction coefficient [88]. No direct correlation was observed between surface roughness and friction coefficient, possibly due to the influence of multiple factors on wear performance [89]. Ferreira *et al*. [90] investigated the wear performance of LPBF-processed H13 steel and 18Ni300 steel after quenching and tempering using a pin-on-disc configuration where H13 steel and 18Ni300 steel were employed as pins. The higher hardness of the H13 steel compared to the 18Ni300 steel had a higher wear resistance and a lower wear rate. The effect of different post-treatments on the wear performance of LPBF-processed H13 steel has not been explored. Furthermore, it is necessary to investigate whether microstructural evolution, such as the formation of tribo-oxide layers and work hardening, affects wear resistance during the wear process. Here, we describe the wear performance of LPBF-processed H13 steel. A thorough investigation of the currently available literature on the wear characteristics of LPBF-processed steels reveals that the research is still in the early stages [1].

4.2.2. Maraging steels (18Ni300 tool steel)

The effect of heat treatment, building direction and sliding velocity on the wear performance of LPBF-processed 18Ni300 steel was studied. It is a common conclusion that higher hardness correlates with better friction resistance [72,91]. The wear mechanism transitions from abrasion wear in the as-built state with low hardness to adhesion wear in the aging state with high hardness [72]. There is controversy about whether microstructural uniformity affects wear performance. Tonolini *et al*. [92] believed that the hardness of LPBF-processed 18Ni300 steel had a greater effect on the wear resistance than the microstructural homogeneity. The hardness of conventionally manufactured 18Ni300 steel after solution and aging was comparable to that of LPBF-processed 18Ni300 steel treated by direct aging. Despite noticeable differences in microstructure, both samples exhibited similar wear rates. However, Godec *et al*. [91] thought the microstructural homogeneity played an important impact on the wear resistance. Fig. 17 illustrates that the LPBF-processed 18Ni300 steel with solution and aging treatment, the LPBF-processed 18Ni300 steel with direct aging treatment, and the conventionally manufactured 18Ni300 steel exhibited similar hardness. However, the conventionally manufactured 18Ni300 steel exhibited the lowest wear rate, and the LPBF-processed 18Ni300 steel with direct aging treatment exhibited the highest wear rate. The presence of a high volume fraction of retained austenite may weaken the wear resistance [91]. Podgornik *et al*. [93] also found that the wear resistance of 18Ni300 built in the horizontal direction and subjected to in-plane sliding was superior to that of samples formed with the vertical build direction and vertical plane combination. This was attributed to the presence of a more homogeneous microstructure and a lower number of interfacial defects within each individual layer. Post-treatments, such as solution aging and plasma nitriding, can not only enhance the hardness of the alloy but also achieve a uniform microstructure, both of which can contribute to improving the wear performance. In addition to the intrinsic properties of the material, wear conditions also play a significant role in determining the wear mechanism and wear resistance [94–95]. Under high load and speed conditions, the frictional heat generated can induce an in-situ tempering effect in the alloy and lead to the formation of an oxide film on the alloy surface, thereby influencing the wear mechanism and performance of the alloy. For example, a smooth and thick tribo-oxide film forms on the worn surface when the sliding speed exceeds 50 m/s. In this case, the wear mechanism is a typical mild oxidative wear. When the load is above 250 N with a sliding speed of 60 m/s, the wear mechanism is severe oxidative or extrusion wear [94]. Additionally, high load and speed easily induce plastic deformation and delamination cracking on the surface of the alloy, which facilitate the generation of debris and accelerate the wear rate [95].

4.3. Thermal properties

4.3.1. Carbon tool steels (H13 tool steel)

For hot working dies, the thermal properties of the materi-

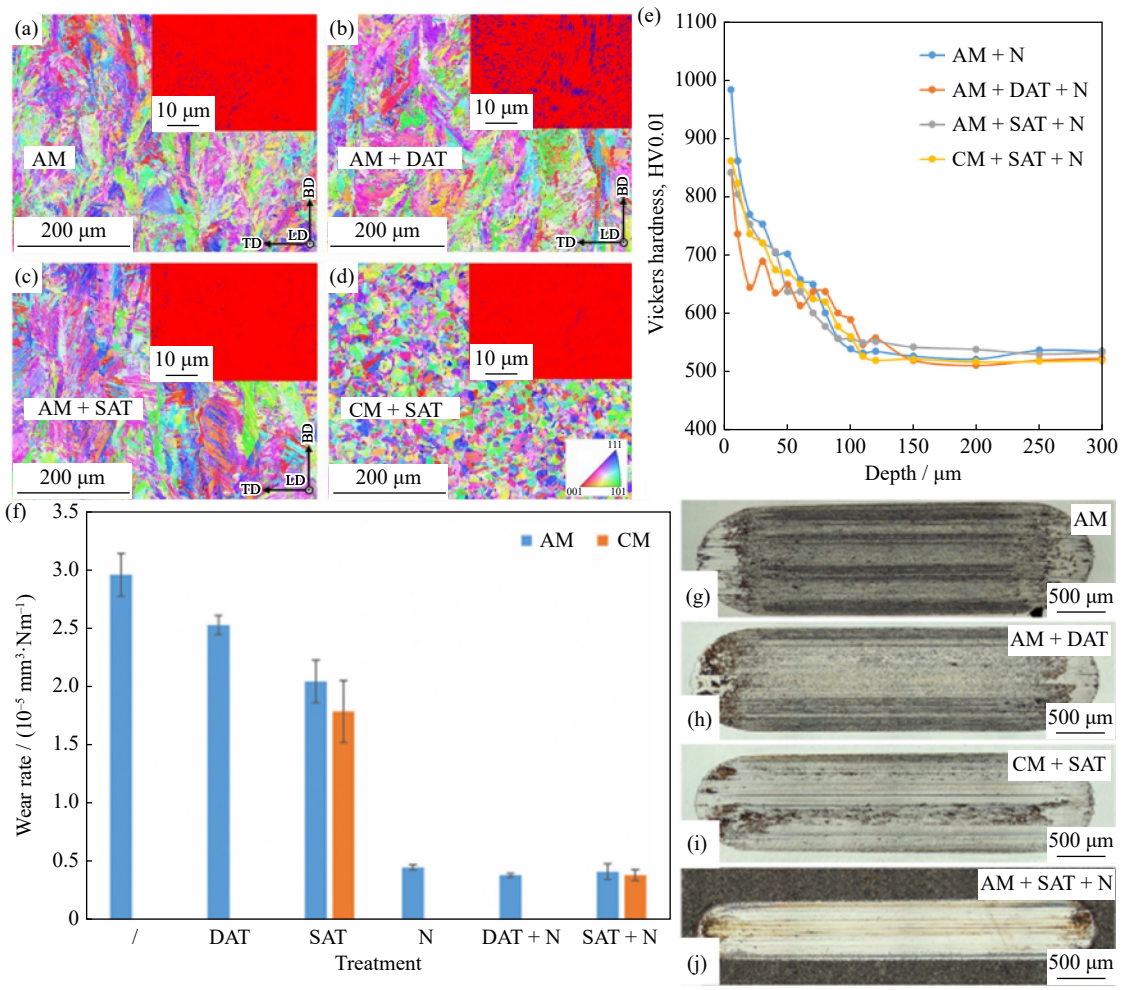

Fig. 17. (a–d) EBSD IPF maps with insets of EBSD phase maps, (e) hardness, (f) wear rate, and (g–j) worn surface of AM, AM + DAT, CM + SAT, and AM + SAT + N samples, respectively (AM: additive manufacturing, CM: conventional manufacturing, DAT: direct aging treatment, SAT: solution and aging treatment, and N: plasma nitriding) [91].

als, such as the coefficient of thermal expansion, thermal diffusivity, specific heat, and thermal conductivity, play an important role in the cooling efficiency and thermal stability of dies. However, for LPBF-processed H13 steel, only the thermal conductivity has been studied in depth. At high temperature, heat transport is primarily carried out by electrons. The thermal conductivity is determined by the interaction between electrons and defects, such as elemental segregation, boundaries, and porosities. The presence of these regions increases electron scattering and reduces thermal conductivity. As depicted in Fig. 18(a) and (d), the samples with high density exhibit enhanced thermal conductivity. The microstructure of the as-built sample consists of martensite and retained austenite, with evident elemental segregation. The thermal conductivity of austenite is much lower than that of martensite, and the region of elemental enrichment increases phonon scattering and decreases thermal conductivity. It can be seen from Fig. 18 that the QT (quenching and double tempering treatment) sample exhibits a more uniform microstructure compared to the DT (direct tempering treatment) sample, resulting in higher thermal conductivity for the QT sample [2]. Although post heat-treatment can enhance the thermal properties, it can also affect the mechanical properties. For example, in the case of H13 steel, the presence of coarse grains resulting from solution treatment may lead to a decrease in strength. Therefore, during post-heat treatment, not only the thermal properties but also the mechanical properties need to be considered. There are few studies on the thermal expansion, thermal diffusivity, and specific heat of LPBF-processed H13 steel, and further exploration is needed. Džugan *et al.* [96] explored the effect of the build directions on the coefficient of thermal expansion, thermal diffusivity, specific heat and thermal conductivity of LPBF-processed H13 steel. The thermal conductivity of H13 steel is primarily associated with microstructural defects. Thermal expansion refers to the change in volume of a material with temperature variation and can reflect the phase transition process, including the ferrite-austenite transformation during the heating process and the martensite transformation during the cooling process. There is limited research on the thermal diffusivity and specific heat of LBF-processed H13 steel, and further investigation is needed.

4.3.2. Maraging steels (18Ni300 tool steel)

The thermal expansion and thermal conductivity of the 18Ni300 steel were explored. The thermal expansion behavior of 18Ni300 steel was related to the phase transition, resid-

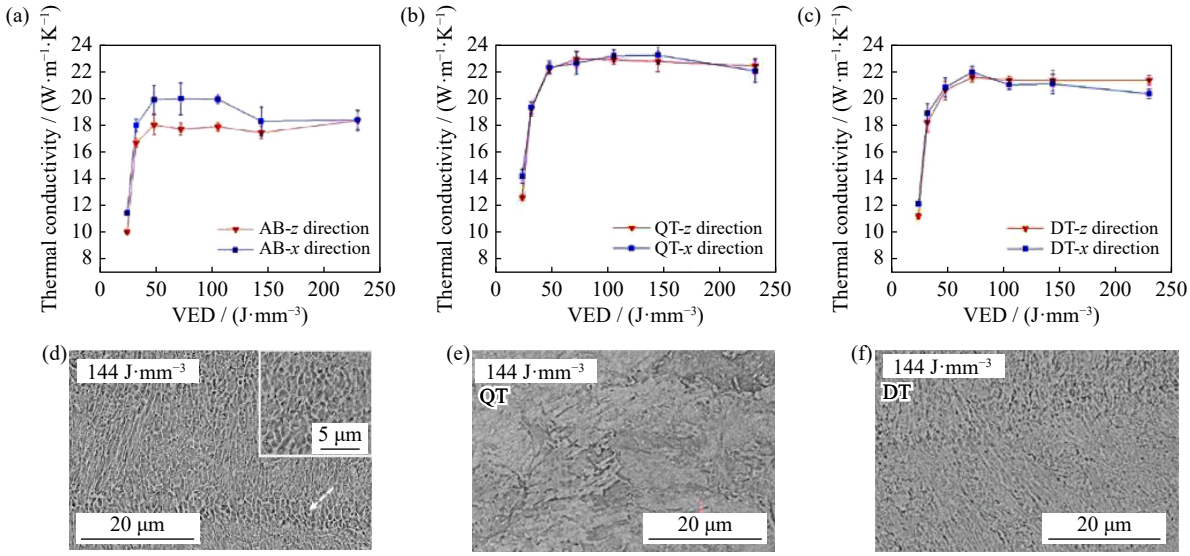

Fig. 18. Thermal conductivities and microstructures of LPBF-processed H13 steel: (a, d) as-built; (b, e) QT; (c, f) DT states [2].

ual stress, microstructure, and texture. The precipitation behavior and austenite reversion reduced the volume during the heating process, as depicted in Fig. 19. The higher volume fraction of martensite transformed to austenite on the OZ sample resulted in a difference in thermal expansion between the OX and OZ samples during the heating process. This discrepancy in thermal expansion behavior between the OX and OZ samples was eliminated after solution treatment. The solution treatment not only eliminated microstructural inhomogeneity but also residual stress. The residual compressive stress was released and expanded to a normal state during the heating process, while the residual tensile stress had the opposite effect. In addition, the texture also plays an impact on the thermal expansion. The <100> texture with a low

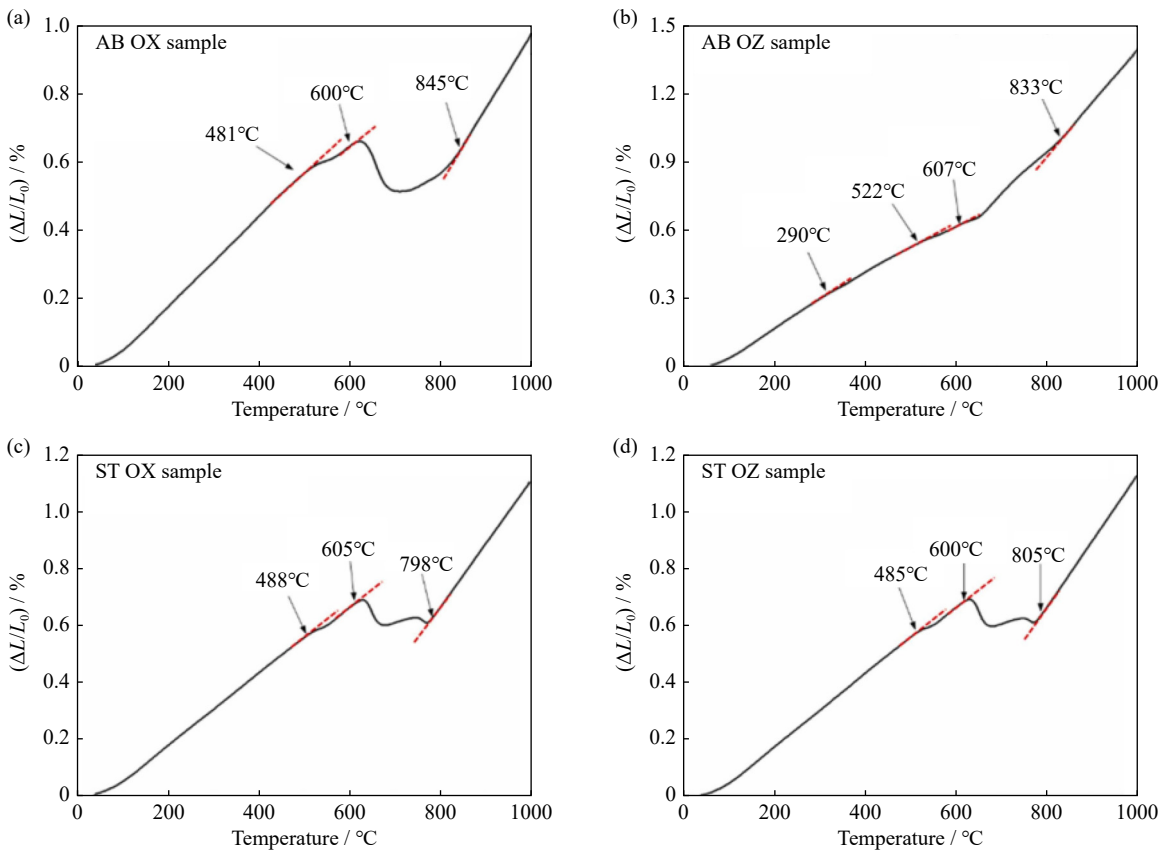

Fig. 19. Thermal expansion curves of the as-built LPBF-processed 18Ni300 steel along the (a) OX direction and (b) OZ direction; thermal expansion curves of the solution treated LPBF-processed 18Ni300 steel along the (c) OX direction and (d) OZ direction. Reprinted from *Addit. Manuf.*, 53, Y.C. Bai, C.L. Zhao, J.Y. Zhang, and H. Wang, Abnormal thermal expansion behaviour and phase transition of laser powder bed fusion maraging steel with different thermal histories during continuous heating, 102712, Copyright 2022, with permission from Elsevier.

elasticity modulus has a higher thermal expansion compared with the <110> texture [97]. Jarfors *et al*. [98] also verified that the thermal expansion was inversely proportional to the material elastic stiffness. In addition to the thermal expansion properties of LPBF-processed 18Ni300 steel, the thermal diffusivity, specific heat, and thermal conductivity were studied [98–99]. For the thermal conductivity, the presence of defects increased electron scattering and decreased thermal conductivity, which was the same as H13 steel. For instance, the direct aging treatment resulted in a reduction in thermal conductivity. This can be attributed to the aging treatment not only failing to eliminate microstructural inhomogeneity but also promoting particle precipitation and a significant volume fraction of austenite formation. The solution treatment increased the thermal conductivity by eliminating molten pool boundaries and microstructural inhomogeneity. The grain size increased and the density of martensite lath boundaries decreased after solution and aging treatment, which further contributed to an increase in thermal conductivity [99]. The thermal diffusivity was higher in the horizontally textured plane than in the textureless build direction. However, an extensive investigation into the underlying factors causing the differences in thermal diffusivity was not carried out. The specific heat is related to the volume fraction of different phases [98].

The thermal conductivity and thermal expansion behavior of the H13 steel and 18Ni300 steel have been systematically discussed. However, further research on thermal diffusivity and specific heat has not yet been conducted in depth. From the above, by adjusting the process parameters and applying post-treatments, it is possible to control the microstructural and defect characteristics to adjust the thermal properties. However, it is important to note that while manipulating the thermal properties, it may also impact other properties of the alloy, such as its tensile property.

5. Conclusions

In summary, the LPBF process offers significant potential for manufacturing parts with intricate structures that would be challenging to produce using conventional methods. The unique thermal history involved in LPBF leads to distinct microstructural characteristics and properties in tool steels compared to those manufactured conventionally. This paper presents a comprehensive overview of the microstructural characteristics and properties exhibited by tool steels in the context of the LPBF process.

(1) Maraging tool steels with ductile martensite can be more easily produced with full density. Conversely, carbon-bearing tool steels with brittle martensite are prone to develop cracks due to residual stress and martensite transformation caused by rapid cooling and a high temperature gradient. Preheating the substrate reduces the temperature gradient and enables the achievement of fully dense carbon-containing tool steels.

(2) In the LPBF process, the high cooling rate, high temperature gradient, and repeated thermal cycles induced the formation of fine grains, different phase constitutions (martensite and retained austenite), cellular substructures, and nanoprecipitates in the tool steels. The martensite transformation results in a weak texture in the tool steels. The fine grains and special cellular substructures can enhance the tensile strength of LPBF-processed tool steels. The intrinsic HT effect in the LPBF process has a minimal influence, leading to fewer nanoprecipitates and a weak precipitation strengthening effect. Process parameter optimization and post-treatments can be employed to adjust the volume fraction, morphology, and size of precipitates to improve strength.

(3) The formation mechanism of retained austenite and its impact on tensile properties remain contentious. In carbon-bearing steel, residual austenite enhances ductility and effectively inhibits crack propagation through the TRIP effect. However, the residual austenite in the maraging steel does not effectively impede crack propagation or induce the TRIP effect. The behavior of residual austenite can vary in different alloy systems, depending on the characteristics of the austenite phase and its interaction with other phases.

(4) Based on a thorough examination of the current literature on the wear behavior of LPBF-processed tool steels, it is clear that this research field is still in its early stages. The wear behavior is influenced by the hardness, microstructural characteristics (microstructural homogeneity), and presence of defects. The wear resistance could be enhanced by increasing their strength and hardness through post-heat treatment and plasma nitriding. Furthermore, variations in friction conditions, such as sliding velocity and temperature, can have a notable effect on the wear mechanism exhibited by the tool steels.

(5) The thermal properties of LPBF-processed tool steels include thermal expansion, thermal diffusivity, specific heat, and thermal conductivity. The thermal conductivity and thermal expansion behavior have been explored. The presence of regions within tool steels that increase electron scattering, such as porosities, grain boundaries, and elemental segregation, can result in a reduction in thermal conductivity. The thermal expansion behavior was related to the phase transition, residual stress, microstructure, and texture. Further exploration is needed to determine the thermal diffusivity and specific heat of the LPBF-processed tool steels.

6. Outlook

Previous studies have contributed to our understanding of the microstructural evolution and the interplay between physical phenomena, microstructural evolution, and properties in LPBF-processed tool steels. The properties of LPBF-processed tool steel are significantly influenced by microstructural characteristics, defects, and residual stress. These factors are determined by the process conditions during manufacturing and the post-treatment procedures applied to the material. To expand the scope of applications and improve the quality of LPBF-processed tool steels, there are still unresolved disagreements and challenges that need to be addressed.

(1) Identify the process-microstructure-property relationship of LPBF-processed tool steels. Under various process parameter conditions, different physical phenomena give rise to a diverse range of microstructures. For instance, altering the preheating temperatures can lead to variations in phase compositions and volume fractions. The alteration of the elemental composition and volume fraction of the constituent phases influences the mechanical properties of the components. Understanding the microstructural evolution under various process parameters and the impact of different phases on the mechanical properties is crucial for precise control of the microstructures and properties of LPBF-processed tool steels.

(2) Emphasize the importance of wear resistance and thermal properties. Currently, there is limited research on wear behavior and thermal properties. However, in the case of tool steels utilized in molds, wear is the primary failure mechanism, and thermal properties significantly affect the forming quality of workpieces and the production efficiency of molds. Enhancing our understanding of wear behavior and thermal properties can facilitate the design and production of tool steels with superior performance.

(3) Develop post-treatment systems for LPBF-processed tool steels to achieve excellent overall performance, including improvements in mechanical and thermal properties, as well as the elimination of defects generated during the LPBF process. Although various post-treatments have been developed to enhance the performance of LPBF-processed tool steel, these methods do not improve the overall performance. The solution and aging treatment can enhance the strength and thermal properties of LPBF-processed H13 steel while concurrently reducing its plasticity. A suitable post-treatment not only enhances the performance of the part but also reduces the cost of production.

(4) Design tool steels specifically tailored for the LPBF process. The existing tool steels can be successfully produced with fully dense structures and desirable properties in the LPBF process through process parameter adjustments. The elemental composition of these tool steels is tailored for the conventional casting process, which may not be suitable for the LPBF process. For instance, the high carbon content in carbon-bearing tool steels can readily lead to crack formation. Hence, it is imperative to design innovative tool steels that not only exhibit excellent LPBF processability but also effectively utilize the unique thermal history of the LPBF process, characterized by high cooling rates and repeated thermal cycles, to achieve superior properties.

(5) Finally, further research should be conducted on real engineering components. The ultimate goal of investigating LPBF-processed tool steels is to fabricate molds featuring intricate conformal cooling channels. Although most studies utilize samples with simple shapes, it is important to note that diverse structures significantly impact the quality and properties of the formed parts.

Acknowledgements

The authors are grateful for the financial supports provided by the China Scholarship Council (Nos. 202206290061 and 202206290062).).

Conflict of Interest

The authors declare that they have no known competing financial interests or personal relationships that could have appeared to influence the work reported in this paper.

References

[1] S.R. Narasimharaju, W.H. Zeng, T.L. See, *et al*., A comprehensive review on laser powder bed fusion of steels: Processing, microstructure, defects and control methods, mechanical properties, current challenges and future trends, *J. Manuf. Process.*, 75(2022), p. 375.

[2] Y.W. Sun, J.L. Wang, M.L. Li, *et al*., Thermal and mechanical properties of selective laser melted and heat treated H13 hot work tool steel, *Mater. Des.*, 224(2022), art. No. 111295.

[3] E.A. Jägle, Z.D. Sheng, P. Kürnsteiner, S. Ocylok, A. Weisheit, and D. Raabe, Comparison of maraging steel micro- and nanostructure produced conventionally and by laser additive manufacturing, *Materials*, 10(2016), No. 1, art. No. 8.

[4] T. DebRoy, H.L. Wei, J.S. Zuback, *et al*., Additive manufacturing of metallic components–Process, structure and properties, *Prog. Mater. Sci.*, 92(2018), p. 112.

[5] H. Fayazfar, M. Salarian, A. Rogalsky, *et al.*, A critical review of powder-based additive manufacturing of ferrous alloys: Process parameters, microstructure and mechanical properties, *Mater. Des*., 144(2018), p. 98.

[6] S. Feng, A.M. Kamat, and Y. Pei, Design and fabrication of conformal cooling channels in molds: Review and progress updates, *Int. J. Heat Mass Transfer*, 171(2021), art. No. 121082.

[7] P.S. Cook and A.B. Murphy, Simulation of melt pool behaviour during additive manufacturing: Underlying physics and progress, *Addit. Manuf.*, 31(2020), art. No. 100909.

[8] P. Bajaj, A. Hariharan, A. Kini, P. Kürnsteiner, D. Raabe, and E.A. Jägle, Steels in additive manufacturing: A review of their microstructure and properties, *Mater. Sci. Eng. A*, 772(2020), art. No. 138633.

[9] E.B. Fonseca, A.H.G. Gabriel, L.C. Araújo, P.L.L. Santos, K.N. Campo, and E.S.N. Lopes, Assessment of laser power and scan speed influence on microstructural features and consolidation of AISI H13 tool steel processed by additive manufacturing, *Addit. Manuf.*, 34(2020), art. No. 101250.

[10] J.T. Wang, S.P. Liu, Y.P. Fang, and Z.R. He, A short review on selective laser melting of H13 steel, *Int. J. Adv. Manuf. Technol.*, 108(2020), No. 7, p. 2453.

[11] Q.Y. Tan, Y. Yin, F. Wang, *et al*., Rationalization of brittleness and anisotropic mechanical properties of H13 steel fabricated by selective laser melting, *Scripta Mater.*, 214(2022), art. No. 114645.

[12] L.L. Guo, L.N. Zhang, J. Andersson, and O. Ojo, Additive manufacturing of 18% nickel maraging steels: Defect, structure and mechanical properties: A review, *J. Mater. Sci. Technol.*, 120(2022), p. 227.

[13] C.L. Tan, K.S. Zhou, W.Y. Ma, P.P. Zhang, M. Liu, and T.C. Kuang, Microstructural evolution, nanoprecipitation behavior and mechanical properties of selective laser melted high-performance grade 300 maraging steel, *Mater. Des.*, 134(2017), p. 23.

[14] Y. Yin, Q.Y. Tan, M. Bermingham, N. Mo, J.Q. Zhang, and M.X. Zhang, Laser additive manufacturing of steels, *Int. Mater. Rev.*, 67(2022), No. 5, p. 487.

[15] K. Chadha, Y. Tian, K. Nyamuchiwa, J. Spray, and C. Aranas

Jr, Austenite transformation during deformation of additively manufactured H13 tool steel, *Mater. Today Commun.*, 33(2022), art. No. 104332.

[16] M. Markl and C. Körner, Multiscale modeling of powder bed-based additive manufacturing, *Annu. Rev. Mater. Res.*, 46(2016), p. 93.

[17] Z.D. Zhang, Y.Z. Huang, A.R. Kasinathan, *et al*., 3-Dimensional heat transfer modeling for laser powder-bed fusion additive manufacturing with volumetric heat sources based on varied thermal conductivity and absorptivity, *Opt. Laser Technol.*, 109(2019), p. 297.

[18] J.P.M. Cheloni, E.B. Fonseca, A.H.G. Gabriel, and É.S.N. Lopes, The transient temperature field and microstructural evolution of additively manufactured AISI H13 steel supported by finite element analysis, *J. Mater. Res. Technol.*, 19(2022), p. 4583.

[19] M. Bayat, W. Dong, J. Thorborg, A.C. To, and J.H. Hattel, A review of multi-scale and multi-physics simulations of metal additive manufacturing processes with focus on modeling strategies, *Addit. Manuf.*, 47(2021), art. No. 102278.

[20] B.C. Liu, R. Wildman, C. Tuck, I. Ashcroft, and R. Hague, Investigaztion the effect of particle size distribution on processing parameters optimisation in selective laser melting process, [in] *2011 International Solid Freeform Fabrication Symposium*, Austin, 2011.

[21] J. Tan, W.L.E. Wong, and K. Dalgarno, An overview of powder granulometry on feedstock and part performance in the selective laser melting process, *Addit. Manuf.*, 18(2017), p. 228.

[22] Y. Liu, J. Zhang, and Z.C. Pang, Numerical and experimental investigation into the subsequent thermal cycling during selective laser melting of multi-layer 316L stainless steel, *Opt. Laser Technol.*, 98(2018), p. 23.

[23] T. Mukherjee, H.L. Wei, A. De, and T. DebRoy, Heat and fluid flow in additive manufacturing—Part I: Modeling of powder bed fusion, *Comput. Mater. Sci.*, 150 (2018), p. 304.

[24] T.N. Le and Y.L. Lo, Effects of sulfur concentration and Marangoni convection on melt-pool formation in transition mode of selective laser melting process, *Mater. Des.*, 179(2019), art. No. 107866.

[25] X.F. Xiao, C. Lu, Y.S. Fu, X.J. Ye, and L.J. Song, *Progress on Experimental Study of Melt Pool Flow Dynamics in Laser Material Processing*, IntechOpen, London, 2021.

[26] S.A. Khairallah, A.T. Anderson, A.M. Rubenchik, and W.E. King, Laser powder-bed fusion additive manufacturing: Physics of complex melt flow and formation mechanisms of pores, spatter, and denudation zones, *Acta Mater.*, 108(2016), p. 36.

[27] O. Zinovieva, A. Zinoviev, and V. Ploshikhin, Three-dimensional modeling of the microstructure evolution during metal additive manufacturing, *Comput. Mater. Sci.*, 141(2018), p. 207.

[28] A.R. Dezfoli, W.S. Hwang, W.C. Huang, and T.W. Tsai, Determination and controlling of grain structure of metals after laser incidence: Theoretical approach, *Sci. Rep.*, 7(2017), art. No. 41527.

[29] P. Ninpetch, P. Kowitwarangkul, S. Mahathanabodee, P. Chalermkarnnon, and P. Rattanadecho, Computational investigation of thermal behavior and molten metal flow with moving laser heat source for selective laser melting process, *Case Stud. Therm. Eng.*, 24(2021), art. No. 100860.

[30] J.H. Li, X.L. Zhou, M. Brochu, N. Provatas, and Y.F. Zhao, Solidification microstructure simulation of Ti–6Al–4V in metal additive manufacturing: A review, *Addit. Manuf.*, 31(2020), art. No. 100989.

[31] Y.P. Lian, S. Lin, W.T. Yan, W.K. Liu, and G.J. Wagner, A parallelized three-dimensional cellular automaton model for grain growth during additive manufacturing, *Comput. Mech.*, 61(2018), No. 5, p. 543.

[32] Y. Zhang and J. Zhang, Modeling of solidification microstructure evolution in laser powder bed fusion fabricated 316L stainless steel using combined computational fluid dynamics and cellular automata, *Addit. Manuf.*, 28(2019), p. 750.

[33] M.A. Kottman, *Additive Manufacturing of Maraging 250 Steels for the Rejuvenation and Repurposing of Die Casting Tooling* [Dissertation], Case Western Reserve University, Cleveland , 2015.

[34] P. Stoll, A. Spierings, K. Wegener, S. Polster, and M. Gebauer, SLM processing of 14Ni (200 grade) maraging steel, [in] *Proceedings of the 3rd Fraunhofer Direct Digital Manufacturing Conference*, Berlin, 2016, p. 6.

[35] P. Kürnsteiner, M.B. Wilms, A. Weisheit, P. Barriobero-Vila, E.A. Jägle, and D. Raabe, Massive nanoprecipitation in an Fe–19Ni–*x*Al maraging steel triggered by the intrinsic heat treatment during laser metal deposition, *Acta Mater.*, 129(2017), p. 52.

[36] Z.H. Liu, D.Q. Zhang, C.K. Chua, and K.F. Leong, Crystal structure analysis of M2 high speed steel parts produced by selective laser melting, *Mater. Charact.*, 84(2013), p. 72.

[37] J. Saewe, C. Gayer, A. Vogelpoth, and J.H. Schleifenbaum, Feasability investigation for laser powder bed fusion of high-speed steel AISI M50 with base preheating system, *BHM Berg Hüttenmänn. Monatsh.*, 164(2019), No. 3, p. 101.

[38] R. Casati, M. Coduri, N. Lecis, C. Andrianopoli, and M. Vedani, Microstructure and mechanical behavior of hot-work tool steels processed by selective laser melting, *Mater. Charact.*, 137(2018), p. 50.

[39] T. Pinomaa, I. Yashchuk, M. Lindroos, T. Andersson, N. Provatas, and A. Laukkanen, Process-structure-properties-performance modeling for selective laser melting, *Metals*, 9(2019), No. 11, art. No. 1138.

[40] J.J. Yan, D.L. Zheng, H.X. Li, *et al*., Selective laser melting of H13: Microstructure and residual stress, *J. Mater. Sci.*, 52(2017), No. 20, p. 12476.

[41] M. Narvan, K.S. Al-Rubaie, and M. Elbestawi, Process–structure–property relationships of AISI H13 tool steel processed with selective laser melting, *Materials*, 12(2019), No. 14, art. No. 2284.

[42] R.A. Savrai, D.V. Toporova, and T.M. Bykova, Improving the quality of AISI H13 tool steel produced by selective laser melting, *Opt. Laser Technol.*, 152(2022), art. No. 108128.

[43] J. Krell, A. Röttger, K. Geenen, and W. Theisen, General investigations on processing tool steel X40CrMoV5-1 with selective laser melting. *J. Mater. Process. Technol.* , 255(2018), p. 679.

[44] R. Mertens, B. Vrancken, N. Holmstock, Y. Kinds, J.P. Kruth, and J. Van Humbeeck, Influence of powder bed preheating on microstructure and mechanical properties of H13 tool steel SLM parts, *Phys. Procedia*, 83(2016), p. 882.

[45] F. Deirmina, N. Peghini, B. AlMangour, D. Grzesiak, and M. Pellizzari, Heat treatment and properties of a hot work tool steel fabricated by additive manufacturing, *Mater. Sci. Eng. A*, 753(2019), p. 109.

[46] F. Lei, T. Wen, F.P. Yang, *et al*., Microstructures and mechanical properties of H13 tool steel fabricated by selective laser melting, *Materials*, 15(2022), No. 7, art. No. 2686.

[47] C.J. Chen, K. Yan, L.L. Qin, *et al*., Effect of heat treatment on microstructure and mechanical properties of laser additively Manufactured AISI H13 tool steel, *J. Mater. Eng. Perform.*, 26(2017), No. 11, p. 5577.

[48] C. Liu, Z.B. Zhao, D.O. Northwood, and Y.X. Liu, A new empirical formula for the calculation of MS temperatures in pure iron and super-low carbon alloy steels, *J. Mater. Process. Technol.*, 113(2001), No. 1-3, p. 556.

[49] M.J. Holzweissig, A. Taube, F. Brenne, M. Schaper, and T. Niendorf, Microstructural characterization and mechanical performance of hot work tool steel processed by selective laser

melting, *Metall. Mater. Trans. B*, 46(2015), No. 2, p. 545.
[50] N. Panahi, M. Åsberg, C. Oikonomou, and P. Krakhmalev, Effect of preheating temperature on the porosity and microstructure of martensitic hot work tool steel manufactured with L-PBF, *Procedia CIRP*, 111(2022), p. 166.
[51] B. Ren, D.H. Lu, R. Zhou, Z.H. Li, and J.R. Guan, Preparation and mechanical properties of selective laser melted H13 steel, *J. Mater. Res.*, 34(2019), No. 8, p. 1415.
[52] G. Huang, K.W. Wei, and X.Y. Zeng, Microstructure and mechanical properties of H13 tool steel fabricated by high power laser powder bed fusion, *Mater. Sci. Eng. A*, 858(2022), art. No. 144154.
[53] Q.Y. Tan, H.W. Chang, Y. Yin, *et al*., Simultaneous enhancements of strength and ductility of a selective laser melted H13 steel through inoculation treatment, *Scripta Mater.*, 219(2022), art. No. 114874.
[54] Y.M. Wang, T. Voisin, J.T. McKeown, *et al*., Additively manufactured hierarchical stainless steels with high strength and ductility, *Nat. Mater.*, 17(2018), No. 1, p. 63.
[55] K. Prashanth and J. Eckert, Formation of metastable cellular microstructures in selective laser melted alloys, *J. Alloys Compd.*, 707(2016), p. 27.
[56] J. Lee, J. Choe, J. Park, *et al*., Microstructural effects on the tensile and fracture behavior of selective laser melted H13 tool steel under varying conditions, *Mater. Charact.*, 155(2019), art. No. 109817.
[57] T. Wen, F.P. Yang, J.Y. Wang, H.L. Yang, J.W. Fu, and S.X. Ji, Ultrastrong and ductile synergy of additively manufactured H13 steel by tuning cellular structure and nano-carbides through tempering treatment, *J. Mater. Res. Technol.*, 22(2023), p. 157.
[58] M. Wang, W. Li, Y. Wu, *et al*., High-temperature properties and microstructural stability of the AISI H13 hot-work tool steel processed by selective laser melting, *Metall. Mater. Trans. B*, 50(2019), No. 1, p. 531.
[59] L.X. Han, Y. Wang, S. Liu, *et al*., Effect of cryogenic treatment on the microstructure and mechanical properties of selected laser melted H13 steel, *J. Mater. Res. Technol.*, 21(2022), p. 5056.
[60] A.F. de Souza, K.S. Al-Rubaie, S. Marques, B. Zluhan, and E.C. Santos, Effect of laser speed, layer thickness, and part position on the mechanical properties of maraging 300 parts manufactured by selective laser melting, *Mater. Sci. Eng. A*, 767(2019), art. No. 138425.
[61] A. Suzuki, R. Nishida, N. Takata, M. Kobashi, and M. Kato, Design of laser parameters for selectively laser melted maraging steel based on deposited energy density, *Addit. Manuf.*, 28(2019), p. 160.
[62] J. Song, Q. Tang, Q.X. Feng, *et al*., Effect of remelting processes on the microstructure and mechanical behaviours of 18Ni-300 maraging steel manufactured by selective laser melting, *Mater. Charact.*, 184(2022), art. No. 111648.
[63] J.K. Ong, Q. Tan, A. Silva, *et al*., Effect of process parameters and build orientations on the mechanical properties of maraging steel (18Ni-300) parts printed by selective laser melting, *Mater. Today Proc.*, 70(2022), p. 438.
[64] N. Takata, R. Nishida, A. Suzuki, M. Kobashi, and M. Kato, Crystallographic features of microstructure in maraging steel fabricated by selective laser melting, *Metals*, 8(2018), No. 6, art. No. 440.
[65] J. Mutua, S. Nakata, T. Onda, and Z.C. Chen, Optimization of selective laser melting parameters and influence of post heat treatment on microstructure and mechanical properties of maraging steel, *Mater. Des.*, 139(2018), p. 486.
[66] J. Suryawanshi, K.G. Prashanth, and U. Ramamurty, Tensile, fracture, and fatigue crack growth properties of a 3D printed maraging steel through selective laser melting, *J. Alloys Compd.*, 725(2017), p. 355.
[67] F. Conde, J. Escobar, J. Oliveira, A. Jardini, W.B. Filho, and J. Avila, Austenite reversion kinetics and stability during tempering of an additively manufactured maraging 300 steel, *Addit. Manuf.*, 29(2019), art. No. 100804.
[68] J. Song, Q, Tang, H. Chen, *et al*. , Laser powder bed fusion of high-strength maraging steel with concurrently enhanced strength and ductility after heat treatments, *Mater. Sci. Eng. A*, 854(2022), art. No. 143818.
[69] Z. Mao, X. Lu, H. Yang, X. Niu, L. Zhang, and X. Xie, Processing optimization, microstructure, mechanical properties and nanoprecipitation behavior of 18Ni300 maraging steel in selective laser melting, *Mater. Sci. Eng. A*, 830(2022), art. No. 142334.
[70] Y.C. Bai, Y.Q. Yang, D. Wang, and M.K. Zhang, Influence mechanism of parameters process and mechanical properties evolution mechanism of maraging steel 300 by selective laser melting, *Mater. Sci. Eng. A*, 703(2017), p. 116.
[71] S. Bodziak, K.S. Al-Rubaie, L.D. Valentina, *et al*., Precipitation in 300 grade maraging steel built by selective laser melting: Aging at 510°C for 2 h, *Mater. Charact.*, 151(2019), p. 73.
[72] S. Yin, C.Y. Chen, X.C. Yan, *et al*., The influence of aging temperature and aging time on the mechanical and tribological properties of selective laser melted maraging 18Ni-300 steel, *Addit. Manuf.*, 22(2018), p. 592.
[73] C.L. Tan, K.S. Zhou, M. Kuang, W.Y. Ma, and T.C. Kuang, Microstructural characterization and properties of selective laser melted maraging steel with different build directions, *Sci. Technol. Adv. Mater.*, 19(2018), No. 1, p. 746.
[74] E.A. Jägle, P.P. Choi, J. Van Humbeeck, and D. Raabe, Precipitation and austenite reversion behavior of a maraging steel produced by selective laser melting, *J. Mater. Res.*, 29(2014), No. 17, p. 2072.
[75] M. Katancik, S. Mirzababaei, M. Ghayoor, and S. Pasebani, Selective laser melting and tempering of H13 tool steel for rapid tooling applications, *J. Alloys Compd.*, 849(2020), art. No. 156319.
[76] M.W. Yuan, Y. Cao, S. Karamchedu, *et al*., Characteristics of a modified H13 hot-work tool steel fabricated by means of laser beam powder bed fusion, *Mater. Sci. Eng. A*, 831(2022), art. No. 142322.
[77] M. Åsberg, G. Fredriksson, S. Hatami, W. Fredriksson, and P. Krakhmalev, Influence of post treatment on microstructure, porosity and mechanical properties of additive manufactured H13 tool steel, *Mater. Sci. Eng. A*, 742(2019), p. 584.
[78] T. Hermann Becker and D. Dimitrov, The achievable mechanical properties of SLM produced Maraging steel 300 components, *Rapid Prototyp. J.*, 22(2016), No. 3, p. 487.
[79] Z.J. Zhao, C.F. Dong, D.C. Kong, *et al*., Influence of pore defects on the mechanical property and corrosion behavior of SLM 18Ni300 maraging steel, *Mater. Charact.*, 182(2021), art. No. 111514.
[80] W. Wu, X. Wang, Q. Wang, *et al*., Microstructure and mechanical properties of maraging 18Ni-300 steel obtained by powder bed based selective laser melting process, *Rapid Prototyping J.*, 26(2020), No. 8, p. 1379.
[81] K. Kempen, E. Yasa, L. Thijs, J.P. Kruth, and J. Van Humbeeck, Microstructure and mechanical properties of selective laser melted 18Ni-300 steel, *Phys. Procedia*, 12(2011), p. 255.
[82] R. Casati, J. Lemke, A. Tuissi, and M. Vedani, Aging behaviour and mechanical performance of 18-Ni 300 steel processed by selective laser melting, *Metals*, 6(2016), No. 9, p. 218.
[83] B. Mooney, K.I. Kourousis, and R. Raghavendra, Plastic anisotropy of additively manufactured maraging steel: Influence of the build orientation and heat treatments, *Addit. Manuf.*, 25(2019), p. 19.
[84] Y.J. Wang, Z. Jia, J.J. Ji, B.L. Wei, Y.B. Heng, and D.X. Liu, Determining the wear behavior of H13 steel die during the ex-

trusion process of pure nickel, *Eng. Fail. Anal.*, 134(2022), art. No. 106053.

[85] S.Q. Wang, M.X. Wei, F. Wang, and Y.T. Zhao, Transition of elevated-temperature wear mechanisms and the oxidative delamination wear in hot-working die steels, *Tribol. Int.*, 43(2010), No. 3, p. 577.

[86] A. Bahrami, S.H.M. Anijdan, M.A. Golozar, M. Shamanian, and N. Varahram, Effects of conventional heat treatment on wear resistance of AISI H13 tool steel, *Wear*, 258(2005), No. 5-6, p. 846.

[87] S. Li, X.C. Wu, S.H. Chen, and J.W. Li, Wear resistance of H13 and a new hot-work die steel at high temperature, *J. Mater. Eng. Perform.*, 25(2016), No. 7, p. 2993.

[88] E. Guenther, M. Kahlert, M. Vollmer, T. Niendorf, and C. Greiner, Tribological performance of additively manufactured AISI H13 steel in different surface conditions, *Materials*, 14(2021), No. 4, art. No. 928.

[89] Z.F. Zhang, L.C. Zhang, and Y.W. Mai, Particle effects on friction and wear of aluminium matrix composites, *J. Mater. Sci.*, 30(1995), No. 23, p. 5999.

[90] D.F.S. Ferreira, J.S. Vieira, S.P. Rodrigues, G. Miranda, F.J. Oliveira, and J.M. Oliveira, Dry sliding wear and mechanical behaviour of selective laser melting processed 18Ni300 and H13 steels for moulds, *Wear*, 488-489(2022), art. No. 204179.

[91] M. Godec, B. Podgornik, A. Kocijan, Č. Donik, and D.A.S. Balantič, Use of plasma nitriding to improve the wear and corrosion resistance of 18Ni-300 maraging steel manufactured by selective laser melting, *Sci. Rep.*, 11(2021), No. 1, art. No. 3277.

[92] P. Tonolini, L. Marchini, L. Montesano, M. Gelfi, and A. Pola, Wear and corrosion behavior of 18Ni-300 maraging steel produced by laser-based powder bed fusion and conventional route, *Procedia Struct. Integr.*, 42(2022), p. 821.

[93] B. Podgornik, M. Šinko, and M. Godec, Dependence of the wear resistance of additive-manufactured maraging steel on the build direction and heat treatment, *Addit. Manuf.*, 46(2021), art. No. 102123.

[94] K. Sun, W.X. Peng, B.H. Wei, L.L. Yang, and L. Fang, Friction and wear characteristics of 18Ni(300) maraging steel under high-speed dry sliding conditions, *Materials*, 13(2020), No. 7, art. No. 1485.

[95] K.C. Bae, D. Kim, Y.H. Kim, *et al.*, Effect of heat treatment, building direction, and sliding velocity on wear behavior of selectively laser-melted maraging 18Ni-300 steel against bearing steel, *Wear*, 482-483(2021), art. No. 203962.

[96] J. Džugan, K. Halmešová, M. Ackermann, M. Koukolíková, and Z.Trojanová, Thermo-physical properties investigation in relation to deposition orientation for SLM deposited H13 steel, *Thermochim. Acta*, 683(2020), art. No. 178479.

[97] Y.C. Bai, C.L. Zhao, J.Y. Zhang, and H. Wang, Abnormal thermal expansion behaviour and phase transition of laser powder bed fusion maraging steel with different thermal histories during continuous heating, *Addit. Manuf.*, 53(2022), art. No. 102712.

[98] A.E.W. Jarfors, T. Matsushita, D. Siafakas, and R. Stolt, On the nature of the anisotropy of maraging steel (1.2709) in additive manufacturing through powder bed laser-based fusion processing, *Mater. Des.*, 204(2021), art. No. 109608.

[99] Y.C. Bai, Y.J. Lee, C.J. Li, and H. Wang, Densification behavior and influence of building direction on high anisotropy in selective laser melting of high-strength 18Ni–Co–Mo–Ti maraging steel, *Metall. Mater. Trans. A*, 51(2020), No. 11, p. 5861.